REPORT DOCUMENTATION PAGE

Form Approved
OMB No. 0704-0188

Public reporting burden for this collection of information is estimated to average 1 hour per response, including the time for reviewing instructions, searching existing data sources, gathering and maintaining the data needed, and completing and reviewing the collection of information. Send comments regarding this burden estimate or any other aspect of this collection of information, including suggestions for reducing this burden, to Washington Headquarters Services, Directorate for Information Operations and Reports, 1215 Jefferson Davis Highway, Suite 1204, Arlington, VA 22202-4302, and to the Office of Management and Budget, Paperwork Reduction Project (0704-0188), Washington, DC 20503.

1. AGENCY USE ONLY (Leave blank)	2. REPORT DATE	3. REPORT TYPE AND DATES COVERED
	30 Sept 94	Final Technical, 1 June 93 - 31 May 94

4. TITLE AND SUBTITLE
Materials for High-Power Laser Applications: Point Defects in KTP and $ZnGeP_2$

5. FUNDING NUMBERS
62102F
2423/67

6. AUTHOR(S)
Larry E. Halliburton

7. PERFORMING ORGANIZATION NAME(S) AND ADDRESS(ES)
Physics Department
West Virginia University
Morgantown, WV 26506-6315

8. PERFORMING ORGANIZATION REPORT NUMBER
AFOSR-TR-95-0295

9. SPONSORING/MONITORING AGENCY NAME(S) AND ADDRESS(ES)
Air Force Office of Scientific Research
Bolling Air Force Base, DC
and
Wright Laboratory/Materials Directorate
Wright-Patterson Air Force Base, OH

NE

10. SPONSORING/MONITORING AGENCY REPORT NUMBER
Grant No.
F49620-93-1-0473

11. SUPPLEMENTARY NOTES

DTIC
SELECTED
DISTRIBUTION CODE
JUN 21 1995
F

12a. DISTRIBUTION/AVAILABILITY STATEMENT
Approved for public release.
Distribution unlimited.

19950616 097

13. ABSTRACT (Maximum 200 words)

The operation of devices utilizing nonlinear optical materials such as KTP and $ZnGeP_2$ are limited at high laser power by point defects in the crystals. This project has used electron paramagnetic resonance (EPR) and electron-nuclear double resonance (ENDOR) experimental techniques to identify and characterize the primary point defects in KTP, $ZnGeP_2$, and $CdGeAs_2$ crystals. In KTP, the primary electron trap (i.e., a Ti^{3+} ion) is associated with the formation of gray tracks. The present investigation has shown that these Ti^{3+} ions have a significantly different local environment depending on whether the crystal was grown hydrothermally or by the flux technique. Also, in KTP, it is shown that potassium vacancies are the primary hole trapping site at low temperature. The acceptor in as-grown crystals of $ZnGeP_2$ is shown to be a singly ionized zinc vacancy or a zinc ion on a germanium site. Results in $CdGeAs_2$ suggest that the dominant EPR-active defects are either a cation vacancy or a cation antisite.

DTIC QUALITY INSPECTED 5

14. SUBJECT TERMS		15. NUMBER OF PAGES
nonlinear optical materials electron paramagnetic resonance electron-nuclear double resonance	gray tracks in KTP point defects KTP, $ZnGeP_2$, $CdGeAs_2$	53 16. PRICE CODE

17. SECURITY CLASSIFICATION OF REPORT	18. SECURITY CLASSIFICATION OF THIS PAGE	19. SECURITY CLASSIFICATION OF ABSTRACT	20. LIMITATION OF ABSTRACT
Unclassified	Unclassified	Unclassified	Unclassified

Accesion For
NTIS CRA&I ☑
DTIC TAB ☐
Unannounced ☐
Justification .....
By .....
Distribution /
Availability Codes
Dist | Avail and / or Special
A-1

TABLE OF CONTENTS

I. EXECUTIVE SUMMARY

This document is the final technical report for work performed under Air Force Office of Scientific Research (AFOSR) Grant F49620-93-1-0473. The title of the project was "Materials for High-Power Laser Applications: Point Defects in KTP and $ZnGeP_2$ Crystals" and the Principal Investigator was Larry E. Halliburton, Physics Department, West Virginia University. This was a one-year research program to use electron paramagnetic resonance (EPR) and electron-nuclear double resonance (ENDOR) techniques to identify and characterize point defects in KTP, $ZnGeP_2$, and $CdGeAs_2$ crystals. During the grant's active period, from June 1, 1993 to May 31, 1994, four major studies were completed and published. These are:

1. Effect of Crystal Growth on Ti^{3+} Centers in $KTiOPO_4$, M. P. Scripsick, G. J. Edwards, L. E. Halliburton, R. F. Belt, and G. M. Loiacono, J. Appl. Phys. 76, 773 (1994).

2. Identification of a Radiation-Induced Hole Center in $KTiOPO_4$, G. J. Edwards, M. P. Scripsick, L. E. Halliburton, and R. F. Belt, Phys. Rev. B 48, 6884 (1993).

3. Electron Paramagnetic Resonance Study of a Native Acceptor in As-Grown $ZnGeP_2$, M. H. Rakowsky, W. K. Kuhn, W. J. Lauderdale, L. E. Halliburton, G. J. Edwards, M. P. Scripsick, P. G. Schunemann, T. M.Pollak, M. C. Ohmer, and F. K. Hopkins, Appl. Phys. Lett. 64, 1615 (1994).

4. Electron Paramagnetic Resonance Spectra in As-Grown $CdGeAs_2$, L. E. Halliburton, G. J. Edwards, P. G. Schunemann, and T. M. Pollock, J. Appl. Phys.(scheduled for Jan. 1, 1995 issue).

In the first of these studies, a series of Ti^{3+} centers were formed in hydrothermally grown and flux-grown potassium titanyl phosphate ($KTiOPO_4$ or KTP). These $3d^1$ defects (S = 1/2) were created with 60-kV x-rays at 77 K, and electron paramagnetic resonance (EPR) and electron-nuclear double resonance (ENDOR) data were taken below 30 K. The ENDOR spectra show that the two Ti^{3+} centers having the largest concentrations in hydrothermally grown KTP have a neighboring proton, presumably in the form of an adjacent OH^- ion. In contrast, ENDOR spectra show that neither of the two Ti^{3+} centers having the largest concentrations in flux-grown KTP have a neighboring proton.

These significant differences in the local environment of the Ti^{3+} centers help explain why KTP crystals have shown differing susceptibilities to gray tracking.

In the second study, electron paramagnetic resonance (EPR) and electron-nuclear double resonance (ENDOR) techniques were used to determine the structure of a radiation-induced trapped-hole center in potassium titanyl phosphate ($KTiOPO_4$ or KTP). A single crystal of KTP was irradiated with 60-kV x-rays at 77 K to produce the S = 1/2 hole center. Data were then taken near 30 K. Spin-Hamiltonian parameters describing the g matrix and three ^{31}P hyperfine matrices were obtained from the angular dependence of the EPR and ENDOR spectra, respectively. The principal values of the g matrix are 2.0008, 2.0250, and 2.0422 and the principal values of the largest phosphorus interaction are -6.809 MHz, -8.125 MHz, and -3.848 MHz. An analysis of the spin-Hamiltonian matrices (i.e., the magnitudes of their principal values and the directions of their principal axes) leads to a model wherein the hole is localized on a bridging oxygen ion between two titanium ions. The hole is stabilized at this site by a nearest-neighbor potassium vacancy. This defect is observed in both hydrothermally grown and flux-grown KTP, and it is stable only up to approximately 160 K.

In the third study, electron paramagnetic resonance (EPR) was used to investigate an acceptor in as-grown single crystals of $ZnGeP_2$. The spectra are characterized by equally spaced triplets with 1:2:1 intensity ratios representing hyperfine interactions (varying from 35 to 55 G in magnitude) with two equivalent phosphorus nuclei. Their angular dependence shows that there are four crystallographically equivalent orientations of the defect. The principal values of the g matrix are 2.002, 2.021, and 2.074 and the corresponding principal axes, at one of the four sites, are the [011], $[\bar{1}00]$, and $[0\bar{1}1]$ directions, respectively. Two possible models are suggested for this acceptor; either a zinc vacancy (V_{Zn}) or a zinc ion on a germanium site (Zn_{Ge}). It also is suggested that the acceptor responsible for the EPR signal is the same acceptor, namely AL1, that gives rise to a dominant near-infrared absorption band.

In the fourth study, electron paramagnetic resonance (EPR) was used to investigate point defects in a single crystal of as-grown $CdGeAs_2$. Spectra taken at 17 K with the magnetic field parallel to the c axis show a broad signal (~165 gauss wide) centered on $g_c = 2.018$ and a sharper signal (~56 gauss wide) centered on $g_c = 2.015$. Together, these signals represent an unpaired-spin concentration of approximately 5×10^{19} cm^{-3}. A single broad signal (~165 gauss wide) centered on $g_a = 1.995$ is observed at 17 K when

the magnetic field is along the a axis. It is suggested that these dominant EPR-active defects in $CdGeAs_2$ consist of either a cation vacancy or an antisite cation with the unpaired spin shared by the four neighboring As ions. Additional weak EPR lines appear when the temperature is increased (from 17 to 40 K) and the microwave power is decreased (from 7 to 2.3 mW).

The results obtained during these four studies are described in detail in this final technical report for AFOSR Grant F49620-93-1-0473.

II. EFFECT OF CRYSTAL GROWTH ON Ti^{3+} CENTERS IN KTP

Titanium ions are the primary electron traps in potassium titanyl phosphate ($KTiOPO_4$), better known as KTP. In this lattice, the titaniums normally occur as closed-shell Ti^{4+} ions (ignoring covalent effects) and they are converted to Ti^{3+} ions upon trapping an electron. The Ti^{3+} ions have a $3d^1$ electron configuration, thus resulting in S = 1/2 centers that are easily observed with electron paramagnetic resonance (EPR) and electron-nuclear double resonance (ENDOR) techniques. In addition to their magnetic properties, Ti^{3+} centers typically have one or more characteristic optical absorption bands in the visible and a broad emission band in the near infrared.

Interest in the Ti^{3+} electron traps has arisen because of their suggested role in the optical damage process in KTP.[1,2] Gray tracks can be observed in many KTP crystals if they are exposed to high-power lasers while used as a frequency-doubler. The laser power density needed to induce gray tracks varies from sample to sample, and this suggests that the gray-tracking phenomenon is dependent on the nature and quantity of point defects present in a particular sample. The Ti^{3+} centers with their broad optical absorption bands in the visible are obvious candidates for the defects involved in gray tracks.

Few details are known about the Ti^{3+} centers in KTP. Roelofs[1] observed EPR spectra from four distinct Ti^{3+} centers in flux-grown material. These defects were produced by electric fields or by annealing in a hydrogen atmosphere. Andreev and Efimov[3] reported seeing these same four centers after room-temperature x-ray irradiation of a flux-grown crystal. Scripsick et al.[4] observed a quite different Ti^{3+} center in hydrothermally grown material after an x-ray irradiation at 77 K. These Ti^{3+} centers, plus others not yet reported in the literature, have different g matrices and different superhyperfine interactions; however, no information has been provided about the differences in the environments that surround the Ti^{3+} centers.

In this section, we describe the results of an ENDOR survey of Ti^{3+} centers in hydrothermally grown and flux-grown KTP crystals. This experimental technique uses hyperfine interactions with neighboring nuclei to probe the surroundings of a paramagnetic defect.[5] We find significant differences in the local environment of the Ti^{3+} centers, and we suggest that this information may help explain why KTP crystals have differing susceptibilities to gray-tracking.

The hydrothermally grown crystals were provided by Airtron (a Division of Litton) in Charlotte, North Carolina, and the flux-grown crystals were provided by Crystal Associates in Waldwick, New Jersey. Samples for the EPR and ENDOR experiments were cut from the larger as-grown boules. The faces of these samples were perpendicular to the three high-symmetry directions (i.e., the **a**, **b**, and **c** axes) and their dimensions were approximately 3 x 3 x 4 mm^3.

The KTP samples were irradiated at 77 K with x-rays to produce the Ti^{3+} centers. Irradiations lasted up to four hours with the x-ray tube operating at 60 kV and 30 mA. After irradiation, the sample was transferred without warming into an Oxford Instruments ESR-900 helium gas flow system for the subsquent EPR or ENDOR measurements. A Bruker ESP 300 spectrometer was used for both the EPR and ENDOR measurements. This spectrometer operated at 9.4 GHz with 100-kHz static field modulation in the EPR mode and with frequency modulation of the rf at 12.5 kHz in the ENDOR mode.

A. Defect Production Mechanism

Although the Ti^{3+} centers described in this section were produced by ionizing radiation (i.e., x-rays), it is expected that similar Ti^{3+} centers will be produced by an intense laser beam, thus making our results directly relevant to the gray tracking problem.[6] An advantage of using x-rays is the increase in the total number of centers that can be made available for study, i.e., defect formation occurs in a larger volume of crystal. Also, producing and studying the defects at 77 K eliminates the significant thermal decay of these centers that occurs at higher temperatures.

Our expectation that x-rays and intense laser beams create the same types of Ti^{3+} centers in KTP comes from the following arguments. Both methods of defect production (x-rays or lasers) begin with the formation of electron-hole pairs in the otherwise perfect lattice. Many of the electrons and holes will immediately recombine, either radiatively or non-radiatively, to restore the perfect lattice; however, a portion of the electrons and holes will migrate sufficiently far from each other and encounter a stabilizing entity, either a vacancy or an extrinsic impurity. Thus, a few of the electrons and holes will become stabilized at widely separated sites within the crystal and form the point defects that contribute to an induced visible optical absorption (e.g., gray tracking). In general, the holes will be localized on an oxygen ion with a neighboring entity, such as a potassium vacancy, providing the stabilizing force.[7] The electrons, on the other hand, will be

localized on a titanium ion with a neighboring entity, such as an OH^- ion or an oxygen vacancy, providing the stabilizing force.

The electron-hole pair needed to initiate damage will be created in the bulk of the crystal whenever above-band-gap photons are present. Ionizing photons are obviously present in the case of x-ray irradiation, but there is some uncertainty as to how a near-infrared laser, such as a 1.06-μm beam from a Nd-YAG laser, would produce photons with energies greater than the band gap. The most likely scenario involves nonlinear processes to achieve wavelengths at or above the band gap (for example, tripling the fundamental beam or sum-frequency generation with a fundamental and a doubled beam). Either of these processes allow a 1.064-μm beam to form 355-nm photons which, coincidently, nearly match KTP's room-temperature band edge at 350 nm.[8] It is important to note that these nonlinear processes, when associated with electron-hole production, do not require phase matching conditions to be satisfied. An above-band-gap photon would immediately create an electron-hole pair very near the site where the photon was formed (or it will be absorbed via other mechanisms) and would not propagate significant distances through the lattice or join with other photons to form a coherent beam.

B. EPR and ENDOR Results

In this investigation, a series of Ti^{3+} centers were produced in hydrothermally grown KTP crystals by x-irradiations at 77 K. Following the example of Roelofs, we label these centers as A, B, etc. and add a subscript *hyd* to identify the center as appearing in hydrothermally grown crystals. Figure 1 shows representative EPR spectra from the two centers having the greatest intensity after irradiation. The spectrum in Fig. 1(a) was taken at 28 K with the magnetic field parallel to the b axis of the crystal. It is centered on 3695.24 G and has a g_b value of 1.8321. Except for a different orientation of magnetic field, this is the same center described in the earlier EPR study by Scripsick et al.[4] We now refer to this center as Center A_{hyd}. The resolved hyperfine pattern associated with this center is explained by interactions with four I = 1/2 nuclei. Application of the ENDOR technique provides precise values for these hyperfine splittings and, most important, it unambiguously identifies the responsible nuclei. The ENDOR spectrum in Fig. 2 was taken at 15 K while monitoring the EPR spectrum in Fig. 1(a). It clearly identifies the responsible nuclei in Center A_{hyd} as three phosphorus and one hydrogen and it gives first-order b-axis hyperfine splittings of 14.68 MHz for the hydrogen nucleus and 11.23 MHz, 17.58 MHz, and 29.02 MHz for the three phosphorus nuclei. Additional

pairs of ENDOR lines with spittings of 2.65 MHz and 0.61 MHz represent phosphorus hyperfine interactions that are not resolved in the EPR spectrum.

A second and less intense Ti^{3+} center, present in hydrothermally grown KTP after irradiation at 77 K, is shown in Fig. 1(b). We refer to this center as Center B_{hyd}. These data were taken at 28 K with the magnetic field parallel to the crystal's a axis. This center has a g_a value of 1.8172 and has eight resolved hyperfine lines in its a-axis EPR spectrum. These lines represent interactions with three neighboring I = 1/2 nuclei which the ENDOR technique identifies as one hydrogen and two phosphorus. The a-axis hyperfine splittings for this center, obtained from the ENDOR spectrum, are 11.00 MHz for the hydrogen and 22.88 MHz and 27.89 MHz for the two phosphorus. In addition to these three nuclei, the ENDOR spectrum shows that several distant hydrogens (approximately 7 Å or more away) are weakly interacting with the Ti^{3+} center.

A different series of Ti^{3+} centers were formed in flux-grown KTP during x-ray irradiations at 77 K. The Ti^{3+} defect having the largest concentration corresponds to "Center B" in Roelofs' paper[1] and we expand his notation by adding a subscript *flx* to denote that this center appears in flux-grown crystals. Thus we refer to this center as Center B_{flx}. The EPR spectrum from this center, taken at 25 K with the magnetic field along the b axis, is shown in Fig. 3(a). Its g_b value is 1.8614 and there are resolved hyperfine interactions with three neighboring I = 1/2 nuclei, two of which are degenerate. The corresponding ENDOR spectrum, taken at 15 K and shown in Fig. 4, identifies these three nuclei as phosphorus. More importantly, there are no ENDOR lines which can be assigned to hydrogen. The b-axis hyperfine splittings, from the ENDOR spectrum, are 9.10 MHz for one phosphorus and 23.13 MHz for the other two phosphorus nuclei.

A second radiation-induced Ti^{3+} center in the flux-grown crystals is shown in Fig. 3(b). It corresponds to "Center C" in Roelofs' paper[1] and, thus, in our notation is Center C_{flx}. This center is considerably less intense than the previously described center. The ENDOR technique shows hyperfine interactions with three phosphorus nuclei. There were no ENDOR lines which could be assigned to hydrogen.

Figure 5 shows the infrared absorption spectra, and thus the relative amounts of OH^-, for our particular crystals. There is approximately an order of magnitude more hydrogen in the hydrothermally grown crystal.

C. Conclusions

We have shown that a variety of Ti^{3+} centers can be created at 77 K in KTP. Furthermore, the specific centers formed in a particular crystal depend on which technique was used to grow the crystal (other unidentified factors, of course, may also play a role). Hydrogen is adjacent to the dominant Ti^{3+} centers in hydrothermally grown crystals, but not in flux-grown crystals. This is consistent with the reports of previous investigators that hydrothermally grown crystals contain significantly more hydrogen than flux-grown crystals.[2,9] In general, we expect an OH^- ion will provide the stabilizing influence needed to trap an electron on an adjacent titanium ion. Why this does not occur in the flux-grown crystals is a major question. Also, it is not known what adjacent entity stabilizes the electron on a titanium ion in the flux-grown crystals. The most likely possibility at this time is an oxygen vacancy. Clearly, more detailed ENDOR studies are needed to clarify the nature and role of the stabilizing entities associated with each Ti^{3+} center in KTP.

The observation that a variety of Ti^{3+} centers may exist in this material has significant ramifications in selecting specific KTP crystals for high-power laser applications. These Ti^{3+} centers, and their associated hole traps, will each have a characteristic thermal stability. For example, at room temperature, many of these defects may thermally decay in milliseconds, whereas others may have lifetimes of minutes or even hours. Knowing which centers will form during exposure to an intense laser beam and knowing the thermal stability of those centers may allow a crystal's susceptibility to gray tracking to be predicted. Beyond simply developing selection criteria for gray-track-resistant crystals, it is reasonable to assume that future improvements in the power-handling capabilitity of KTP crystals will focus on the elimination, or neutralization, of those stabilizing entities that allow an electron to be trapped on a titanium. In this last regard, it is important to realize that elimination, or neutralization, of hole trapping sites may be more realistic, and just as effective, as focusing on the elimination of electron traps.

III. IDENTIFICATION OF A RADIATION-INDUCED HOLE CENTER IN KTP

Potassium titanyl phosphate ($KTiOPO_4$), better known as KTP, is widely used to frequency-double infrared lasers into the visible.[10,11] However, point defects, with their associated optical absorption bands, can limit the power-handling capability of these doubler crystals. Optical damage in KTP usually manifests itself as small gray tracks

produced when a crystal is subjected to high-power, high-repetition-rate laser pulses.[12,13,2] The defects responsible for the gray tracking have not been identified, nor has the mechanism by which these defects are formed. Before significant progress can be made in improving the performance of KTP doubler crystals, in-depth studies are needed to identify and characterize the various point defects that can exist in the material. A better understanding of the mechanisms in KTP by which point defects form, stabilize, interact, and decay will then lead to a correlation of gray tracking with specific defects.

Very few investigations of point defects in KTP have been reported thus far. Scripsick et al.[4] observed three paramagnetic radiation-induced point defects in hydrothermally grown KTP. These defects were only stable below room temperature and included a trapped-hole center, a Ti^{3+} center, and a Pt^{3+} center. Roelofs,[1] in a study of flux-grown material, reported four paramagnetic Ti^{3+} centers produced by electric fields or by annealing in a hydrogen atmosphere. After x-ray irradiating flux-grown crystals at room temperature, Andreev and Efimov[3] found an aluminum-related paramagnetic hole center and the four Ti^{3+} centers previously reported by Roelofs. Morris and coworkers[14-16] used ionic conductivity results from KTP to obtain evidence for potassium and oxygen vacancies. Other investigations[17,18,9] have focused on the large number of OH^--related infrared absorption bands in KTP in the 3400 to 3700 cm^{-1} spectral range. In addition, there have been a series of magnetic resonance studies of transition-metal-ion impurities (i.e., Fe^{3+}, Cr^{3+}, and V^{4+}).[19-23]

In this section, we describe the results of a detailed electron paramagnetic resonance (EPR) and electron-nuclear double resonance (ENDOR) investigation of the dominant low-temperature, radiation-induced trapped-hole center in KTP. From the angular dependence of the EPR and ENDOR data, we show that this defect has the hole localized on an oxygen ion between two titaniums and that a nearest-neighbor potassium vacancy serves as the stabilizing entity. This particular defect is the principal hole trap in both hydrothermally grown and flux-grown KTP crystals. Its identification provides spectroscopic evidence, through the EPR technique, for the existence of potassium vacancies in KTP. Also, this defect is expected to play a significant role in the gray-tracking phenomenon because of its relatively long lifetime (i.e., milliseconds) at room temperature.

A. Crystal Structure of KTP

The crystal structure of KTP was initially determined by Tordjman et al.[24] and later verified by Thomas et al..[25] It is orthorhombic with space group $Pna2_1$ and the symmetry elements are two glide planes and one screw axis. A unit cell of this material contains 64 ions and has lattice parameters **a** = 12.819 Å, **b** = 6.399 Å, and **c** = 10.584 Å. The first glide plane consists of a reflection through a plane perpendicular to the **a** axis with subsequent translations of 1/2 the lattice parameter along the **b** and **c** axes. The second glide plane is a reflection through a plane perpendic-ular to the **b** axis with a translation of 1/2 the lattice parameter along the **a** axis. The screw axis is a 180° rotation around the **c** axis with a translation of 1/2 the lattice parameter along the **c** axis.

Titanium ions are found in two crystallographically inequivalent sites within the KTP structure. There also are two distinct sites for the potassium ions and two for the phosphorus ions. The oxygen ions occupy ten crystallographically inequivalent sites. Together, these ions represent 16 distinct sites in the crystal. Their lattice positions are given in Table I, and the positions of the remaining atoms in the unit cell can be generated by applying the symmetry elements of the crystal. Specifically, a second set of 16 ion positions can be generated from the x,y,z values in Table I by applying a transformation representing the first glide plane. The appropriate equations are

$$x' = 1/2 - x, \quad (1a)$$
$$y' = y+1/2, \quad (1b)$$
$$\text{and} \quad z' = z+1/2. \quad (1c)$$

In this and the subsequent transformation, all of the x,y,z values are in units of the a,b,c lattice parameters, respectively. A third set of 16 ion positions can be generated from the x,y,z values in Table I by applying a transformation representing the second glide plane. An appropriate set of equations in this case are

$$x' = x+1/2, \quad (2a)$$
$$y' = 3/2 - y, \quad (2b)$$
$$\text{and} \quad z' = z. \quad (2c)$$

The fourth set of 16 ion positions can be generated by sequentially applying both of the glide plane transformations given above and is equivalent to applying a transformation representing the screw axis alone.

Table I. Ion positions are given in units of the a, b, and c lattice parameters for one-quarter of a unit cell in KTP. The remaining 48 ions in the unit cell are obtained from these by application of the crystal's symmetry elements. [Taken from Ref. 25, except for a different choice of Ti(1) and OT(1).]

Atom	x/a	y/b	z/c
K(1)	0.37807	0.7806	0.6880
K(2)	0.10526	0.6990	0.9332
Ti(1)	0.37290	0.5001	0.9996
Ti(2)	0.24658	0.2695	0.74836
P(1)	0.49808	0.3363	0.7397
P(2)	0.18079	0.5020	0.4872
O(1)	0.4859	0.4867	0.8497
O(2)	0.5103	0.4657	0.6170
O(3)	0.4004	0.1986	0.7208
O(4)	0.5934	0.1930	0.7589
OT(1)	0.2752	0.4653	0.8561
OT(2)	0.2232	0.0413	0.6097
O(5)	0.1126	0.3106	0.4585
O(6)	0.1113	0.6918	0.5117
O(7)	0.2525	0.5402	0.3718
O(8)	0.2528	0.4619	0.6008

B. EPR Results

The crystal used in this study was grown by the hydrothermal technique at Airtron (a Division of Litton) in Morris Plains, New Jersey. Seed temperature during growth was 550°C and nutrient temperature was 570°C. Pressure within the autoclave was 1.72 x 10^8 Pa (i.e., 25,000 psi) and growth time was approximately 40 days. EPR and ENDOR data were taken on a sample 3 x 3 x 4 mm^3 which had been cut from the larger as-grown boule. The faces of this rectangular sample were perpendicular to the three high symmetry directions (i.e., the **a**, **b**, and **c** axes).

The KTP sample was irradiated at 77 K with x-rays to produce the trapped-hole centers. Irradiations lasted up to four hours with the x-ray tube operating at 60 kV and 30 mA. Following an irradiation, the sample was transferred without warming into an Oxford Instruments Model ESR-900 helium gas flow system for the subsequent EPR or ENDOR measurements. The EPR data were taken with a Bruker Model ESP 300 spectrometer operating at 9.440 GHz with 100-kHz static field modulation. A Varian E-500 digital gaussmeter was used to measure the magnetic field and a Hewlett-Packard 5340A counter was used to measure the microwave frequency. A small MgO:Cr crystal was used to correct for the difference in magnetic field between the KTP sample and the gaussmeter probe (the isotropic g value for Cr^{3+} in MgO is 1.9800). The Bruker ESP 300 spectrometer also was used for the ENDOR measurements. In these experiments, the rf field was frequency modulated at 12.5 kHz with the depth of modulation varying from 10 to 50 kHz. The ENDOR coil was helical and was attached to the Oxford Instruments glassware extending through the Bruker ENDOR cavity.

Before irradiation, the KTP sample was visibly clear; after irradiation at 77 K, it had a reddish-brown coloration. Correspondingly, only a weak Fe^{3+} EPR spectrum was present before irradiation, and a very large holelike spectrum was present after the 77-K irradiation. Other EPR spectra, due to Ti^{3+} and Pt^{3+} centers, were present after the irradiation but they are not the focus of this investigation.

The trapped-hole center's EPR spectrum, taken with the magnetic field parallel to the **c** axis of the crystal, is shown in Fig. 6(a). It consists of a primary doublet having a 2.57-G separation and secondary triplets (with 1:2:1 relative intensities) having 0.69-G separations. The g-value along the **c** direction is 2.0300. Based on this **c**-axis spectrum, Scripsick et al.[6] concluded that this was an S = 1/2 defect interacting with three I = 1/2, 100% abundant nuclei. When the magnetic field is along the **a** direction, the spectrum has a g-value of 2.0131 and consists of a doublet split by about 1.5 G. The **b**-direction spectrum has a g-value of 2.0251 and consists of a doublet having a splitting of 2.54 G. These latter two spectra are shown in Figs. 6(b) and 6(c).

Although the trapped-hole center's EPR spectrum is best observed near 30 K, it can be monitored at temperatures above 80 K. At the higher temperatures, the triplet structure observed in Fig. 6(a) is unresolved. Also, below 20 K, there is a broadening which decreases the resolution. If the temperature of the sample rises above approxi-

mately 160 K, the trapped-hole center anneals and the sample must be re-irradiated before continuing with a study of the defect.

For an arbitrary direction of the magnetic field, there are four magnetically inequivalent orientations of the trapped hole center and there are four sets of EPR lines. If the magnetic field is restricted to the **a-c**, **b-c**, or **a-b** planes, the four sites are pairwise degenerate and only two sets of EPR lines are observed. Finally, when the magnetic field is along any of the three high-symmetry axes, all four sites are magnetically equivalent and only a single set of EPR lines is observed (as shown in Fig. 6). In the present investigation, EPR data were taken at approximately 5°-intervals in the **a-c**, **b-c**, and **a-b** planes of the crystal. The observed angular dependence associated with the g-matrix is shown in Fig. 7 where hyperfine splittings are ignored and the data points represent the center of each set of hyperfine-split lines. Although one hyperfine interaction was resolved at a majority of the angles for which EPR data were taken, its analysis is not attempted until the ENDOR data is available later in this section.

The spin-Hamiltonian for an S=1/2, I=1/2 defect is

$$H_s = \beta \mathbf{S} \cdot \mathbf{g} \cdot \mathbf{H} + \mathbf{S} \cdot \mathbf{A} \cdot \mathbf{I} - g_N \beta_N \mathbf{H} \cdot \mathbf{I} \qquad (3)$$

where the terms represents the electron Zeeman interaction, the hyperfine interaction, and the nuclear Zeeman interaction, respectively. A minimum of six parameters (three principal values and three Euler angles specifying the directions of the principal axes) are needed to describe the g matrix and another six are needed for each hyperfine matrix. In this paper, the Euler angles are converted into (θ,φ) pairs of angles, thus making it easier to describe the direction of each principal axis. The polar angle θ is measured relative to the **+c** direction and the azimuthal angle φ is measured relative to the **+a** direction in the **c** plane with positive rotation being from **a** to **b**.

The angular dependence of the EPR spectrum was used to obtain the g-matrix parameters. In particular, a least-squares-fitting program repeatedly diagonalized a 2 x 2 Hamiltonian matrix (representing only the electron Zeeman term) while using 95 independent measurements of EPR line positions and their associated microwave frequencies as input data. These 95 magnetic fields represented the mid-points of sets of hyperfine-split lines (i.e., the data points in Fig. 7). Table II contains the resulting "best-fit" g-matrix parameters. The average deviation between the measured and the final calculated line positions was 0.085 G.

Table II. Spin-Hamiltonian parameters for the trapped-hole center in KTP. The g matrix was obtained from EPR data and the hyperfine matrices were obtained from ENDOR data.

Matrix	Principal values	Principal directions θ	φ
g	2.0008	57.9°	156.8°
	2.0250	79.9°	60.4°
	2.0422	34.1°	315.1°
A_1 (^{31}P)	-6.809 MHz	131.5°	91.6°
	-8.125 MHz	44.3°	66.7°
	-3.848 MHz	77.3°	170.1°
A_2 (^{31}P)	0.918 MHz	72.3°	138.1°
	0.547 MHz	71.6°	234.2°
	2.598 MHz	26.0°	7.2°
A_3 (^{31}P)	0.500 MHz	136.9°	120.0°
	-0.360 MHz	132.6°	310.6°
	2.280 MHz	84.7°	35.7°

The spin-Hamiltonian parameters given in Table II correspond to one of the four crystallographically equivalent sites occupied by the trapped hole center in KTP. All four sites have the same principal values, but the change in directions of the principal axes when going from one site to another must reflect the symmetry elements of the lattice. The sets of angles needed to describe a principal-axis direction at the other three sites are obtained from the initial set as follows:

Site 1:	(θ_1,φ_1)	
Site 2:	$(\theta_1, 180^\circ - \varphi_1)$	Reflection in the **a** plane.
Site 3:	$(\theta_1, 360^\circ - \varphi_1)$	Reflection in the **b** plane.
Site 4:	$(\theta_1, 180^\circ + \varphi_1)$	Reflections in both planes.

Note that a right-hand coordinate system does not survive in these transformations of the directions of principal axes. However, either sense along a specified line describes equally well the direction associated with the corresponding principal value of a spin-Hamiltonian matrix.

C. ENDOR Results

An electron-nuclear double resonance spectrum from the trapped-hole center in KTP is shown in Fig. 8. This spectrum was taken with the magnetic field along the **c** axis and it contains six distinct pairs of lines centered on the free nuclear-resonance frequency (ν_N) of phosphorus. Each of the observed hyperfine interactions is less than the free nuclear-resonance frequency; thus, the ENDOR spectrum consist of pairs of lines separated by A and centered on ν_N. The two ENDOR lines forming the most widely split pair in Fig. 8 are separated by 7.297 MHz and correspond to the phosphorus nucleus responsible for the 2.57-G hyperfine splitting observed in the **c**-axis EPR spectrum (see Fig. 6(a)). A second pair of phosphorus ENDOR lines are separated by 2.232 MHz and a third pair of phosphorus lines are separated by 1.503 MHz. The average of these latter two separations matches the 0.69-G triplet hyperfine splitting observed in Fig. 6(a). Except for an isolated line at 3.188 MHz, the remaining ENDOR lines in Fig. 8 represent phosphorus hyperfine interactions which are unresolved in the EPR spectra.

ENDOR spectra were taken with the magnetic field along the **a**, **b**, and **c** directions, and also at selected orientations of the magnetic field within each of the **a-c**, **b-c**, and **a-b** planes of the crystal. These latter measurements, two in each plane, were made at angles approximately 25° from each of the two high symmetry directions defining the plane. This gave a total of 15 distinct ENDOR spectra, one each for the three high symmetry directions and two each for the six orientations between the high symmetry directions, from which to obtain parameters describing the various phosphorus hyperfine interactions.

The experimentally measured separations of pairs of ENDOR lines representing three of the ^{31}P hyperfine interactions are plotted in Figs. 9 and 10. These three sets of ENDOR data were separately fit using the spin-Hamiltonian given by Eq. (3). Specifically, the 4 x 4 matrix derived from the spin-Hamiltonian was repeatedly diagonalized while the six parameters describing the hyperfine matrix (three principal values and three Euler angles) were varied. This procedure continued until a "best-fit" set of hyperfine

parameters were obtained for each of three nuclei. These results are listed in Table II. The average deviation between the measured and the final calculated values for the separation of pairs of ENDOR lines was 7.5 kHz, 12.5 kHz, and 10.0 kHz, respectively, for the A_1, A_2, and A_3 nuclei. Three additional ^{31}P ENDOR spectra are resolved in Fig. 8, but they were not analyzed in the present investigation.

The following condition was used to choose the absolute signs for the principal values of the A_1, A_2, and A_3 hyperfine matrices in Table II. When a hyperfine matrix is reduced to its isotropic and anisotropic parts (as is done in the next subsection), the anisotropic parameter representing the classic dipole-dipole interaction must have the same sign as the nuclear magnetic moment. This condition forces all three principal values of the A_1 matrix to be negative and leads to the interesting result wherein the isotropic parameter for A_1 has an "anomalous" sign opposite to that of the nuclear magnetic moment. Similar "anomalous" signs for the isotropic hyperfine parameter have been observed for trapped-hole centers in other oxides.[26] The situation is simpler for the A_2 and A_3 matrices where the isotropic and anisotropic parameters have the same sign.

D. Model of the Trapped-Hole Center

The g matrix reported in Table II has a small, but significant, positive shift which strongly suggests that the center is holelike, and thus must be a defect consisting of a missing electron from an oxygen. A hole residing on an oxygen ion (i.e., an O^- ion) in an oxide material typically gives positive g shifts in the range of 0.02 to 0.08. This is easily seen by considering the g values predicted for an unpaired electron occupying an oxygen p orbital in a tetragonal crystal field.[27,5] To first order, these are

$$g_{\parallel} = g_e \qquad (4a)$$

and

$$g_{\perp} = g_e - 2\lambda/\Delta. \qquad (4b)$$

The parameter Δ is the splitting between the singlet and doublet energy levels associated with the three p orbitals and λ is the spin-orbit constant. For an oxygen ion, λ is -135 cm^{-1}. This gives values of 0.5 to 1.5 eV for Δ when the g shifts are in the range of 0.02 to 0.08. In this simple model, Δ is interpreted to be the energy associated with the optical transition from the ground state (p_z) to the first excited state (p_x,p_y) of the O^- ion. However, the optical absorption peak positions observed for hole centers in oxides are usually a factor of two larger than the value of Δ predicted from their measured g shifts.

In the case of the trapped-hole center in KTP, the p orbital containing the unpaired electron is in an orthorhombic crystal field. This causes all three principal values of the g matrix to be unique,[5] in agreement with the results in Table II.

The hyperfine matrices describing the interactions between phosphorus nuclei and the unpaired electron associated with the hole center are given in Table II. It is instructive to decompose each of these hyperfine matrices into an isotropic part and an anisotropic part (i.e., $\mathbf{A} = a\mathbf{I} + \mathbf{B}$). The anisotropic portion **B** can further be represented in its principal-axis system by two interaction constants as follows.[5]

$$\mathbf{B} = \begin{pmatrix} -b+b' & & \\ & -b-b' & \\ & & 2b \end{pmatrix} \qquad (5)$$

In this form, the parameter b' represents the deviation from axial symmetry for the anisotropic interaction. Values for these three hyperfine constants (deduced from the **A** matrices in Table II) are $a_1 = -6.261$ MHz, $b_1 = 1.206$ MHz, and $b_1' = 0.658$ MHz for matrix $\mathbf{A}_1$, they are $a_2 = 1.354$ MHz, $b_2 = 0.622$ MHz, and $b_2' = 0.185$ MHz for matrix $\mathbf{A}_2$, and they are $a_3 = 0.807$ MHz, $b_3 = 0.737$ MHz, and $b_3' = 0.430$ MHz for matrix $\mathbf{A}_3$.

As noted earlier, the g matrix provides evidence that the trapped hole resides on an oxygen ion. It remains to be determined which of the ten inequivalent oxygen ions in the unit cell will trap the hole. Fortunately, the isotropic constant ($a_1 = -6.261$ MHz) extracted from the largest phosphorus hyperfine matrix allows one to significantly narrow the number of possibilities. This isotropic constant is an order of magnitude smaller than the value expected if the oxygen ion containing the hole were a component of a PO_4 group. Supporting evidence for this statement is provided by gamma-irradiated KH_2PO_4 (KDP) where a trapped-hole center, consisting of an unpaired electron localized on an oxygen ion in a PO_4 group, has an observed isotropic phosphorus hyperfine interaction of 96.7 MHz.[28] Thus, because of the small value of the phosphorus isotropic interaction in KTP, the eight oxygen ions directly bonded to phosphorus ions are eliminated as sites for the trapped hole and only the two oxygen ions without an adjacent phosphorus neighbor are left as candidates. These latter two oxygen ions have two titaniums as nearest neighbors.

Additional evidence that places the trapped hole on one of the two oxygen ions that are bonded only to titanium nearest-neighbors comes from the anisotropic part of the largest hyperfine interaction. The parameter b in Eq. (5) can be approximated reasonably well, in our case, by a simple point dipole-dipole interaction. In this approximation, b is related to the dipole separation R by the following expression.[5]

$$b = (\mu_o/8\pi)\, g_n \mu_n g_e \mu_B\, (2/R^3) \qquad (6)$$

A brief calculation shows that a b_1 value of 1.206 MHz corresponds to a separation distance of 2.98 Å between the unpaired electron and the phosphorus nucleus. This distance is quite different from the nominal oxygen-phosphorus separation of 1.54 Å found in the PO_4 groups within KTP. In contrast, the calculated value of 2.98 Å compares favorably with the actual distance (i.e., 3.22 Å to 3.32 Å) from titanium-bridging oxygen ions to their nearest-neighbor phosphorus ions.

A remaining step in developing a model for the trapped-hole center is to explain how the hole is stabilized at a particular oxygen ion. There is no evidence in the literature to support the stable self-trapping of a hole on an oxygen ion in an otherwise perfect oxide lattice. The self-trapping of holes does occur in the alkali halides,[29] but not in oxides. Thus, a trapped-hole center in an oxide crystal includes a component that provides the stabilizing force to maintain the hole at the specific defect site and prevent it from migrating (i.e., hopping) through the lattice. In many oxides, the stabilizing entity is a nearest neighbor cation vacancy,[27] and we suggest a similar explanation for the trapped-hole center in KTP. Specifically, we propose that a potassium vacancy is adjacent to the oxygen ion trapping the hole in KTP. In support of this expectation, we find reasonable agreement between the direction of the unique axis of the g matrix (i.e., the 2.0008 value) and the direction from a titanium-bridging oxygen to a potassium (see Table III).

A trapped-hole center consisting of an O^- ion between two titanium ions with a nearest-neighbor potassium vacancy could exist in four distinct configurations within the KTP lattice. The four possibilities arise because there are two crystallographically inequivalent oxygen sites between titanium ions and there are two crystallographically inequivalent potassium sites. However, only one of the four possibilities provides a good match to the directions of the unique axes of the experimentally measured spin-Hamiltonian matrices. This is shown in Table III where the directions and separations of pairs of

ions in the "perfect" KTP lattice are compared with the unique axes of the **g** matrix and the hyperfine matrices.

Significant lattice relaxation in and around the defect (on the order of 3 to 6%) is expected to accompany the formation of the potassium vacancy and O^- ion, and this will cause the directions of the unique principal axes of the g and hyperfine matrices to deviate by small, but measurable, amounts from the ion-to-ion directions in the perfect lattice. Also, the spatial distribution of the p-orbital wave function occupied by the hole will cause deviations of hyperfine principal axes from the ion-to-ion directions.

Table III. Comparison of directions and ion separations in the KTP crystal structure with experimental directions and separations obtained from the **g** matrix and the hyperfine matrices.

Ion Pair[1] or Principal Axis	Direction θ	Direction φ	Separation Distance[2]
OT(1)----K(2)	72.84°	145.53°	2.765 Å
g-matrix unique axis	57.9°	156.8°	
P(1)------OT(1)	67.50°	163.89°	3.219 Å
$\mathbf{A}_1$-matrix unique axis	77.3°	170.1°	2.98 Å
P(2)------OT(1)	17.52°	349.02°	4.094 Å
$\mathbf{A}_2$-matrix unique axis	26.0°	7.2°	3.72 Å
P^*(1)-----OT(1)	73.05°	28.51°	4.226 Å
$\mathbf{A}_3$-matrix unique axis	84.7°	35.7°	3.52 Å

[1] The position of ion $P^*(1)$ is obtained from ion P(1) by applying the second glide plane (i.e., Eqs. 2) and then translating one unit in the -a direction and one unit in the -b direction.

[2] For the hyperfine principal axes, this separation distance is the classic dipole-dipole prediction as given by Eq. (6).

However, despite these uncertainties associated with lattice relaxations and the lack of corrections for the spatial distribution of the unpaired electron's wave function, the agreement found in Table III provides encouraging support for the following model. Specifically, we propose that the trapped-hole center in KTP consist of a hole (i.e., a missing electron) localized on the OT(1) oxygen ion with a potassium vacancy at the nearest-neighbor K(2) site. This oxygen ion bridges between the Ti(1) and Ti(2) titanium ions, with Ti(1) providing the "long" bond to OT(1) and Ti(2) providing the "short" bond. The largest hyperfine interaction is with the P(1) phosphorus ion, which agrees with the lobe of the p-orbital pointing toward this ion. A schematic representation of this model for the trapped-hole center is shown in Fig. 11. The A_2 and A_3 hyperfine interactions are with the P(2) and $P^*(1)$ phosphorus ions (see Table III for a description of P^*) and both of these ions are joined via oxygen ions to Ti(2). Since Ti(2) represents the "short" bond to OT(1), it is reasonable to expect that more of the spin density will be transferred to the Ti(2) side of the defect rather than to the "long" bond Ti(1) side.

The specific model illustrated in Fig. 11 suggests that only potassium vacancies on the K(2) site, or one of the other three equivalent sites in the unit cell, will trap a hole on an adjacent oxygen ion. This can be explained either by (a) assuming that potassium vacancies in KTP occupy only the K(2) site and not the K(1) site, or (b) assuming that potassium vacancies occupy both sites but holes are only trapped by the vacancies on the K(2) sites. Choice (a) has significant ramifications for the defect structure of KTP, if it is shown to be true by later experiments. Choice (b) is equally likely to be operative since the separation between the oxygen ion and the potassium vacancy is an important parameter in deciding whether the resulting hole center will be thermally stable. As described earlier, there are four combinations of titanium-bridging oxygens and potassium sites in the KTP lattice and their separations are 2.722 Å, 2.765 Å, 2.996 Å, and 3.057 Å in the perfect lattice. The model in Fig. 11 corresponds to the 2.765 Å separation. Subsequent investigations in which the sample is irradiated and maintained at temperatures near that of liquid helium may reveal additional stable configurations of trapped hole centers in KTP.

In concluding this section, we note that a paramagnetic trapped-hole center has been produced in KTP during x-ray irradiation at 77 K. The defect is stable up to 160 K, but its EPR spectrum can best be observed near 30 K. There is a strong hyperfine interaction with one ^{31}P nucleus and weaker interactions with additional ^{31}P nuclei. Parameters for the g matrix and three hyperfine matrices were obtained from the angular

dependence of the EPR and ENDOR spectra, respectively. The g-shifts, the isotropic hyperfine interactions, and the anisotropic hyperfine interactions suggested a model in which the hole is localized on a bridging oxygen ion between two titanium ions. The hole is stabilized at this oxygen by a nearest-neighbor potassium vacancy.

IV. EPR OF A NATIVE ACCEPTOR IN AS-GROWN $ZnGeP_2$

Zinc germanium phosphide ($ZnGeP_2$) is rapidly becoming an important frequency conversion material for the infrared spectral region.[30-34] This material is transparent from near 0.7 to 11 μm and has a large nonlinear optical coefficient, thus making it an excellent candidate for second harmonic generation (SHG) and optical parametric oscillator (OPO) applications. Furthermore, phase matching can be achieved at room temperature across the entire range of transparency. In the past, the development of $ZnGeP_2$-based optical devices has been limited (1) by a lack of large, properly oriented single crystals and (2) by an acceptor-related absorption band in the near infrared extending from approximately 0.7 μm to 2.5 μm. It is only recently, through improved crystal-growth procedures and post-growth anneals, that major progress has been made in overcoming both limitations.[35] These efforts have culminated in several demonstrations of 2.05-μm-pumped Type-I $ZnGeP_2$ OPOs. Budni et al.[36] reported a 26% overall conversion efficiency and a 37% slope efficiency at an average continuous power output of 0.6 W. Schunemann et al.[37] obtained a 1.6-W average output power while maintaining an overall efficiency of 18%.

Additional improvements in the performance of $ZnGeP_2$-based OPOs can be expected if the material's extrinsic absorption near the pump wavelength at 2.05 μm is further reduced. A deep acceptor, recently designated[38] as AL1 (i.e., acceptor level one), is responsible for this near-edge absorption. The AL1 center is present in all $ZnGeP_2$ crystals at concentrations on the order of 10^{19} to 10^{20} cm^{-3}; however, in the past, optical measurements combined with various post-growth treatments have not provided sufficient information to establish a microscopic model for this defect. We have noted that an intense electron-paramagnetic-resonance (EPR) signal[39] from an acceptor also is present in all as-grown $ZnGeP_2$ crystals. It is our expectation that the EPR signal and the AL1 center have a common origin, since they have similar concentrations, both are acceptors, and both can be reduced in intensity by comparable amounts when a crystal is thermally annealed. By focusing on this EPR signal, we hope to better understand the AL1 center.

In this section, we describe the results of a study of the EPR signal which is present in as-grown crystals of $ZnGeP_2$. The initial observation of this signal was reported by Kiel[39] in 1974. We have made a more careful analysis of the EPR spectrum's angular dependence and have found precise principal values and principal axis directions for the g matrix of this center. Our conclusions, which differ considerably from those of Kiel, restrict the most likely model for this acceptor to two choices, either a zinc vacancy (V_{Zn}) or a zinc ion on a germanium site (Zn_{Ge}). The acceptor, in either case, is in a single-negative charge state and the unpaired spin (i.e., the hole) is localized on a pair of adjacent phosphorus atoms. The defect's primary symmetry axis is oriented along [011]-type directions, thus giving it four crystallographically equivalent orientations in the lattice. In contrast, Kiel[39] misinterpreted the angular dependence of the EPR spectrum and erroneously concluded that the pair of phosphorus atoms sharing the hole had their primary symmetry axis along [110]-type directions.

$ZnGeP_2$ has the tetragonal chalcopyrite crystal structure[40] where the **c** direction is denoted as [001] and the two equivalent **a** directions are labeled [100] and [010]. The lattice parameters, $\mathbf{a} = 5.46$ Å and $\mathbf{c} = 10.71$ Å, give a value for c/a of 1.96. Thus, the crystal can be viewed as having an approximate 2% distortion from the simpler zinc-blende structure. In $ZnGeP_2$, each Zn ion and each Ge ion has four P neighbors, and each P ion has two Zn and two Ge neighbors. The GeP_4 units are nearly perfect tetrahedra, whereas the ZnP_4 units form slightly distorted tetrahedra.[40] In particular, the two P-Zn-P angles in the ZnP_4 unit are 108.5^o and 111.4^o, as compared with the perfect tetrahedral bond angle of 109.47^o, whereas the two Ge-P-Ge angles in the GeP_4 unit are 109.3^o and 109.6^o.

A. EPR Results

The single crystals used in this study were grown at Lockheed Sanders by the horizontal gradient freeze technique.[35] They are nearly stoichiometric but may be slightly Ge-rich because of the greater volatility of the zinc at the high growth temperatures. EPR samples, in the form of cubes approximately 2.5 mm on a side, were cut from larger boules. They were oriented such that [100], [010], and [001] directions emerged from the three orthogonal faces. A Bruker ESP-300 spectrometer operating at 9.45 GHz was used to obtain the EPR data. Microwave frequencies and magnetic fields were measured with a Hewlett Packard 5340A counter and a Varian E-500 digital gaussmeter, respective-

ly. A small MgO:Cr crystal was used to correct for the difference in magnetic field between the sample and the gaussmeter probe (the isotropic g value for Cr^{3+} in MgO is 1.9800). An Oxford Instruments ESR-900 helium gas flow system maintained the sample temperature near 20 K during the measurements.

The EPR spectra taken along various high symmetry directions are shown in Fig. 12. Each of these spectra consists of one or more similar triplets (i.e., sets of three lines equally split and having 1:2:1 intensity ratios) which preliminary electron-nuclear double resonance (ENDOR) experiments have shown to be due to equal hyperfine interactions with a pair of phosphorus nuclei. A complete ENDOR study of this defect in $ZnGeP_2$ is in progress and will be reported in a separate paper. The EPR data in Fig. 12 can be described by the S = 1/2 spin-Hamiltonian

$$\mathcal{H} = \beta \mathbf{S}\cdot\mathbf{g}\cdot\mathbf{H} + \mathbf{S}\cdot\mathbf{A}\cdot\mathbf{I}_1 + \mathbf{S}\cdot\mathbf{A}\cdot\mathbf{I}_2$$

where the first term represents the electron-Zeeman interaction and the last two terms represent the phosphorus hyperfine interactions. The focus in this letter is on the electron-Zeeman term and the information provided by the g matrix.

As shown in Fig. 12, the EPR spectrum from this defect consists of a single triplet when the magnetic field is parallel to either the [001] or the [110] directions. In contrast, when the magnetic field is along the [011] direction, there are three distinct triplets with the middle one being twice as intense (i.e., doubly degenerate). Finally, with the magnetic field in the [100] direction, two poorly resolved triplets are present, each doubly degenerate. From this, we deduce that the defect has four crystallographically equivalent orientations in the lattice. All four orientations are magnetically equivalent when the magnetic field is along the [001], [110], or [1$\bar{1}$0] directions, but this degeneracy is partially lifted when the magnetic field is rotated in either the {100} or the {110} sets of planes. If the magnetic field were along an arbitrary direction, the orientational degeneracies would be entirely removed and the EPR spectrum would contain four distinct triplets, although they might be poorly resolved because of the relatively small g shifts.

A g matrix having principal axes along the [011], [$\bar{1}$00], and [0$\bar{1}$1] directions fits the data presented in Fig. 12. Given that the [100]- and [010]-type directions are equal and the [001] direction is unique, there are four possible orientations of this g matrix in the chalcopyrite structure and they correspond to the four crystallographically equivalent

orientations observed in the data. The principal g values associated with these principal-axis directions were obtained as follows. It was noted that the lowest-field triplet in the [011] EPR spectrum had the magnetic field parallel to a principal axis and that the highest field triplet in this same EPR spectrum had the magnetic field along another of the principal axes. The corrected magnetic fields corresponding to the centers of these two triplets are 3256.0 G and 3373.4 G (for a microwave frequency of 9450.70 MHz). These data give 2.074 and 2.002 for the two principal g values. The remaining g value is 2.021 and is obtained from the [110] EPR spectrum where the fourfold degenerate triplet is located at 3328.1 G (for a microwave frequency of 9450.00 MHz). The effective g value for this latter line depends on all three principal g values; however, two of the principal values were already known at this point. These results for the g matrix are summarized in Table IV. It is important to note that the g-shifts associated with this EPR center are positive, thus indicating that the defect is an acceptor.

Table IV. Principal values and principal axes directions of the g matrix for the four crystallographically equivalent defect sites labeled 1 through 4 in Fig. 13.

Principal Values	Principal Axes Directions			
	Site 1	Site 2	Site 3	Site 4
2.002	[011]	[101]	[$\bar{1}$01]	[0$\bar{1}$1]
2.021	[$\bar{1}$00]	[010]	[0$\bar{1}$0]	[100]
2.074	[0$\bar{1}$1]	[$\bar{1}$01]	[101]	[011]

B. Model of the Acceptor

The observed hyperfine interactions (i.e., the triplets) require that the unpaired spin be equally shared between two phosphorus atoms, presumably nearest neighbors. This is consistent with the observation of four crystallographically equivalent orientations of the g matrix. Specifically, four phosphorus atoms surround each cation site (i.e., zinc or germanium) in the chalcopyrite structure, and four pairs of these phos-phorus atoms having the same symmetry as the g matrix can easily be identified. These four pairs,

labeled 1 through 4, are illustrated in Fig. 13. Having the defect occupy only these four crystallographically equivalent sites is not surprising since a close examination of the chalcopyrite structure reveals that the six possible pairs of phosphorus atoms within the tetrahedron shown in Fig. 13 naturally separate into two sets.[40] Four of the pairs have one separation distance and the remaining two pairs have a different separation distance. For example, in a GeP_4 unit, the fourfold-degenerate pairs have separation distances of 3.792 Å and the twofold-degenerate pairs have separation distances of 3.798 Å. The difference between the two types of pairs is even greater in a ZnP_4 unit where the four-fold-degenerate separation is 3.856 Å and the twofold-degenerate separation is 3.924 Å.

Preliminary ENDOR data provide no evidence for the association of an impurity with the defect, and this is consistent with the growth of the crystals from ultra-high-purity (six 9s pure) starting materials. Furthermore, impurities are not expected at the 10^{19} to 10^{20} cm^{-3} levels exhibited by the EPR signal. This restricts the possible models for our paramagnetic center to native defects such as vacancies and antisite atoms. Phosphorus on an antisite can be eliminated from consideration because the observed hyperfine is too small by more than an order of magnitude.[41] The requirement that the unpaired spin be localized on two adjacent phosphorus atoms eliminates zinc on a phosphorus site, germanium on a phosphorus site, and a phosphorus vacancy. Germanium on a zinc site is eliminated because it is a donor. This leaves a zinc on a germanium site, a zinc vacancy, and a germanium vacancy as the possible models for the negative-charged acceptor. The germanium vacancy is an unlikely candidate because the germanium-rich nature of $ZnGeP_2$ crystals suggests that germanium vacancies are not a dominant component of the defect structure in this material. Also, the germanium vacancy is an unlikely candidate because the two separation distances for adjacent phosphorus pairs (where the unpaired spin resides) are only slightly different which makes it likely that all six possible pairs of phosphorus atoms surrounding the vacancy would be occupied, in disagreement with observation. However, lattice relaxation may invalidate this latter argument. In conclusion, we are left with either a zinc vacancy or a zinc on a germanium site as the model for our EPR-active acceptor defect.

ENDOR experiments, focused on the germanium and zinc neighbors, are the only way to determine which of the two proposed models is correct. Until then, both models remain plausible. It is quite possible that both types of defects may be present in the as-grown crystals even though we are observing only one in a paramagnetic form. The higher volatility of zinc during crystal growth could lead to large concentrations of zinc

vacancies. The presence of large numbers of zinc and germanium antisites also is expected since the material solidifies at 1020°C as a zinc-blende random alloy and undergoes a phase transition to the chalcopyrite structure at 952°C. Zinc and germanium ions are randomly distributed over the cation sites in the high-temperature phase, and not all of the disorder is removed when the crystal is cooled below the phase change. Thus, large concentrations of zinc and germanium ions may exist on the wrong cation site even at room temperature. Even though we suggest that germanium antisites may very well exist in the material, we believe it is unlikely they are directly associated with the EPR-active defect being discussed at the present time.

In summary, our model for the EPR-active acceptor defect present in as-grown $ZnGeP_2$ is an unpaired spin (i.e., a hole) shared equally by a pair of phosphorus ions adjacent to either a zinc vacancy or a zinc on a germanium site. The EPR experiments do not distinguish between the two possibilities. Only the four pairs of phosphorus ions having the shorter separation and oriented along [011]-type directions are occupied by the hole. This model is illustrated in Fig. 13 where the four crystallographically equivalent orientations of the acceptor are labeled 1 through 4. At this time, there is no data to suggest whether or not the unpaired spin is hopping between different pairs of phosphorus atoms within a given tetrahedron. Also, there is no evidence concerning the identity of other defects that may be present in the crystal for compensation or to ensure overall charge neutrality.

Thermally annealing an as-grown $ZnGeP_2$ crystal significantly reduces[42] the concentration of the AL1 center and, similarly, we have found that the annealing process also decreases the concentration of the EPR-active acceptor. Thus, it is tempting to suggest that the AL1 center and the acceptor responsible for the EPR signal are the same. Future studies, in which optical absorption and EPR measurements are made on the same samples after irradiation and thermal annealing treatments, will aid in confirming our tentative identification.

V. EPR SPECTRA IN AS-GROWN $CdGeAs_2$

Cadmium germanium arsenide ($CdGeAs_2$) belongs to the ternary chalcopyrite family[30] of nonlinear optical materials. It is a II-IV-V_2 semiconducting compound analogous to the widely studied III-V materials except that its crystal structure is tetragonally distorted from the simpler zinc-blende structure of the III-V compounds. At room tem-

perature, the lattice parameters[43] of $CdGeAs_2$ are **a** = 5.945 Å and **c** = 11.221 Å and the space group for the crystal is $I\bar{4}2d$. The absorption edge[44-46] of $CdGeAs_2$ occurs near 2.34 μm (i.e., 0.53 eV) and its transparency range extends to 17 μm.

The chief interest in $CdGeAs_2$ arises from its extremely large nonlinear optical coefficient. The reported value[47] of 351 pm/V for d_{36} is the highest among known compounds, three times higher than that of $ZnGeP_2$ and nine times higher than $AgGaSe_2$ (two commercially available materials for infrared frequency conversion applications). In addition, $CdGeAs_2$ has sufficient birefrigence to allow phase-matching throughout its transparency range. Although its small band gap precludes the use of $CdGeAs_2$ for most optical-parametric-oscillator applications, the material shows promise for frequency-doubling the output of CO_2 lasers. For example, Iseler et al.[48] achieved up to 27% conversion efficiency and produced almost 2 W of average second-harmonic output power when $CdGeAs_2$ was pumped with a Q-switched, 10.6-μm laser operating at a repetition rate of 20 kHz. Unfortunately, these investigators had to cool the crystal to 77 K to reduce the optical absorption in the mid-infrared.

A major challenge, therefore, in the development of $CdGeAs_2$ crystals for second harmonic generation is the elimination or reduction of defect-related absorption bands in the region of the output wavelength. Isomura et al.,[44] for example, describe an intense absorption shoulder extending out from the band edge in a p-type crystal having a hole concentration of 2×10^{16} cm^{-3}. In a more detailed study characterizing the extrinsic absorption in the 2.5 to 17-μm region, Iseler et al.[48] found that p-type samples could be described by a model consisting of donors (D) of undetermined ionization energy, shallow acceptors (A1) that are closely compensated by the donors, and deep acceptors (A2) located near the center of the energy gap. They observed concentrations of the A2 acceptor ranging from 5×10^{16} to 2×10^{20} cm^{-3} in samples from different growth runs, thus leading them to conclude that this deep acceptor is probably a native defect, rather than an impurity.[48]

The dominant acceptors (and donors) in as-grown material are thought to come from a combination of (1) nonstoichiometry introduced during growth and (2) the incomplete removal of disorder on the cation sublattice during subsequent cool-down. This second mode of defect formation is expected because $CdGeAs_2$ crystals undergo a disorder-to-order phase transition[30] upon cooling through 630°C. In this transition, the crystal goes from the zinc-blende structure (where Cd and Ge randomly fill cation sites)

to the chalcopyrite structure (where Cd and Ge occupy alternating cation sites), and it is quite possible that some residual disorder survives to room temperature. Thus, the optically active point defects in $CdGeAs_2$ are most likely various types of vacancies and antisite ions. Spectroscopic techniques capable of probing the bulk of the crystal, such as photoluminescence and electron paramagnetic resonance (EPR), can be used to identify and monitor these major point defects in $CdGeAs_2$.

In this section, we describe the results of an EPR investigation of as-grown $CdGeAs_2$. The sample used in this study was cut from a large (19-mm diameter by 100-mm length) substantially crack-free single crystal grown at Lockheed Sanders by the horizontal gradient freeze technique. Dimensions of the EPR sample were 2.5 x 2.9 x 2.7 mm^3 along the [100], [010], and [001] directions, respectively. In this tetragonal lattice, the c axis is defined to be the [001] direction and the two equivalent a axes then correspond to the [100] and [010] directions. A Bruker ESP-300 spectrometer operating at 9.45 GHz was used to obtain the EPR data. Microwave frequencies were measured with a Hewlett Packard 5340A counter and magnetic fields were measured with a Varian E-500 digital gaussmeter. A small MgO:Cr crystal was used to correct for the difference in magnetic field between the sample and the gaussmeter probe (the isotropic g value for Cr^{3+} in MgO is 1.9800). An Oxford Instruments ESR-900 helium gas flow system maintained the sample temperature at selected values between 8 and 40 K during the measurements. Special care was taken in cooling and in warming the crystal because of the significant anisotropy in its thermal expansion properties. The coefficient of thermal expansion is reported to be ten times greater for the a axis than the c axis.[49]

There is a broad EPR signal in as-grown $CdGeAs_2$ which can easily be observed when the sample temperature is reduced below 60 K. At higher temperatures, the Q of the microwave cavity is destroyed as a result of absorption associated with free carriers present in the conduction or valence bands of the crystal. The EPR spectrum shown in Fig. 14(a) was taken with the magnetic field along the c axis of the crystal and the spectrum shown in Fig. 14(b) was taken with the magnetic field along the a axis. Spectrometer settings were the same for both traces; the sample temperature was 17 K, the microwave power incident on the cavity was 7 mW, and the amplitude of the 100-kHz modulation was 10 gauss.

In both of the spectra shown in Fig. 14, an intense EPR signal representing approximately 5 x 10^{19} spins/cm^3 is observed near $g \cong 2$. The overall linewidth in both

traces is about 165 gauss, with structure being present in Fig. 14(a) but not in Fig. 14(b). There was no change in the linewidth of the c-axis spectrum as the temperature was reduced from 40 K to 8 K; thus, we attribute the observed linewidth primarily to unresolved hyperfine interactions with the magnetic nuclei surrounding the paramagnetic defects. We cannot, however, rule out contributions to the linewidth from random strain-induced variations either in the g values or in the zero-field splittings (if the spin S is greater than 1/2), but we consider these latter possibilities to be less likely. If hyperfine is responsible for the observed linewidths, a significant contribution would be expected from ^{75}As nuclei (I = 3/2) as a result of their 100% abundance and lesser contributions would be expected from ^{111}Cd and ^{113}Cd nuclei (both I = 1/2) with 12.8% and 12.2% abundance, respectively. Thus far, we have been unsuccessful in obtaining an electron-nuclear double resonance (ENDOR) spectrum from the EPR signals shown in Fig. 14. In general, the ENDOR experiment requires that an EPR transition be saturated (i.e., populations equalized) with microwave power. This, in turn, allows nuclear spin flips to be detected via their effect on the saturated EPR signal. The ENDOR experiments in $CdGeAs_2$ were limited by our inability to saturate the EPR signal, even at 5 K, presumably because of short spin-lattice relaxation times.

Close examination of the structure present on the c-axis spectrum in Fig. 14(a) shows it to be slightly asymmetric. This asymmetry, which is even more apparent in spectra taken at lower microwave powers and higher temperatures, suggests that there are at least two distinct spectra (i.e., two different centers) present in Fig. 14(a). In the simplest interpretation, the c-axis spectrum is described as a sharper line approximately 56 gauss in width superimposed on a broad line 165 gauss in width. The sharper line is slightly offset to higher field and has a g_c value of 2.015 while the broader line has a g_c value of 2.018. When the magnetic field is along the a axis, as in Fig. 14(b), the spectrum consist of a single structureless broad line with $g_a = 1.995$. Presumably, this a-axis spectrum contains unresolved components associated with each of the signals seen in the c-axis spectrum. During rotation of the magnetic field from the c-axis to the a-axis, i.e., going from Fig. 14(a) to Fig. 14(b), the shift of the spectrum occurs gradually and no increased resolution appears at intermediate angles.

Figure 15 shows the c-axis EPR spectrum taken at 41 K with a reduced microwave power of 2.3 mW. When compared to Fig. 14(a), this higher-temperature spectrum has a considerably better resolved structure but a much worse signal-to-noise ratio. The broad underlying line which was dominant in Fig. 14(a) is still observable

near $g \cong 2$, but now there are additional sharper lines superimposed on it and there are small outer satellite lines near 2950, 3100, and 3600 gauss. Weak intensities and overlapping components prevented us from following the angular dependences of these sharper central and satellite lines. It is not yet clear whether these sharper lines arise from a single additional defect or they represent several additional paramagnetic defects. Also, a preliminary examina-tion of intensity ratios and splittings does not support assigning the satellite lines to ^{111}Cd and ^{113}Cd hyperfine interactions.

Our initial survey of EPR spectra in as-grown $CdGeAs_2$ has provided evidence for the presence of several paramagnetic point defects. However, there is not sufficient resolution in the spectra to conclusively identify the specific models of the responsible defects. Based on recent work in other ternary chalcopyrite crystals, we can, nevertheless, tentatively suggest that the primary EPR-active defects in $CdGeAs_2$ are associated with the cation sublattice. Recently, Rakowsky et al.[50] described an EPR spectrum from an acceptor in as-grown $ZnGeP_2$ and suggested that it is either a zinc vacancy (V_{Zn}) or a zinc ion on a germanium site (Zn_{Ge}). The unpaired spin in $ZnGeP_2$ interacts primarily with only two phosphorus nuclei neighboring the cation site and has g values of 2.002, 2.021, and 2.074. This anisotropy in g values corresponds to a Δg of 0.072. In contrast, the present investigation gives a Δg of only 0.023 for the dominant defect(s) in $CdGeAs_2$. The smaller anisotropy in g values observed in $CdGeAs_2$ suggests that the unpaired spin may be shared by the four As ions surrounding the cation site, thus averaging out the anisotropy that would occur if the spin were localized on only one or two of the As neighbors. Also, a rapid hopping, or tunneling, of the spin among the As neighbors would agree with the fast spin-lattice relaxation encountered in our attempts to obtain ENDOR spectra. An additional example of a delocalized spin surrounding a cation vacancy in a ternary chalcopyrite is provided by the recent work of Aksenov et al.[51] They observed a photo-induced, isotropic EPR signal at $g = 2.019$ in $CuAlS_2$ and assigned it to a copper vacancy (V_{Cu}) with the hole equally shared by the four nearest-neighbor sulfur ions. Bardeleben et al.[52] previously had observed a similar copper-vacancy defect in $CuGaS_2$.

REFERENCES

1. M. G. Roelofs, J. Appl. Phys. 65, 4976 (1989).

2. G. M. Loiacono, D. N. Loiacono, T. McGee, and M. Babb, J. Appl. Phys. 72, 2705 (1992).

3. B. V. Andreev and V. N. Efimov, Mod. Phys. Lett. B 6, 177 (1992).

4. M. P. Scripsick, G. J. Edwards, L. E. Halliburton, and R. F. Belt, J. Appl. Phys. 70, 2991 (1991).

5. J. -M. Spaeth, J. R. Niklas, and R. H. Bartram, Structural Analysis of Point Defects in Solids (Springer-Verlag, Berlin, 1992).

6. B. V. Andreev, V. A. Maslov, V. A. Mikhailov, S. K. Pak, O. P. Shaunin, and I. A. Sherbakov, SPIE Vol. 1839, pp. 280-89.

7. G. J. Edwards, M. P. Scripsick, L. E. Halliburton, and R. F. Belt, Phys. Rev. B 48, 6884 (1993).

8. J. C. Jacco and G. M. Loiacono, Appl. Phys. Lett. 58, 560 (1991).

9. P. A. Morris, M. K. Crawford, and B. Jones, J. Appl. Phys. 72, 5371 (1992).

10. F. C. Zumsteg, J. D. Bierlein, and T. E. Gier, J. Appl. Phys. 47, 4980 (1976).

11. J. D. Bierlein and H. Vanherzeele, J. Opt. Soc. Am. B 6, 622 (1989).

12. J. K. Tyminski, J. Appl. Phys. 70, 5570 (1991).

13. N. B. Angert, V. M. Garmash, N. I. Pavlova, and A. V. Tarasov, Sov. J. Quantum Electron. 21, 426 (1991).

14. P. A. Morris, M. K. Crawford, A. Ferretti, R. H. French, M. G. Roelofs, J. D. Bierlein, J. B. Brown, G. M. Loiacono, and G. Gashurov, Mater. Res. Soc. Symp. Proc. 152, 95 (1989).

15. P. A. Morris, M. K. Crawford, M. G. Roelofs, J. D. Bierlein, P. K. Gallagher, G. Gashurov, and G. M. Loiacono, Mater. Res. Soc. Symp. Proc. 172, 283 (1990).

16. M. G. Roelofs, P. A. Morris, and J. D. Bierlein, J. Appl. Phys. 70, 720 (1991).

17. W. M. Theis, G. B. Norris, and M. D. Porter, Appl. Phys. Lett. 46, 1033 (1985).

18. F. Ahmed, R. F. Belt, and G. Gashurov, J. Appl. Phys. 60, 839 (1986).

19. N. M. Nizamutdinov, N. M. Khasanova, G. R. Bulka, V. M. Vinokurov, I. S. Rez, V. M. Garmash, and N. I. Pavlova, Sov. Phys. Crystallogr. 32, 408 (1987).

20. J. F. Stenger, Y. Dusausoy, G. Marnier, H. Rager, and J. M. Gaite, J. Phys.: Condens. Matter 1, 4643 (1989).

21. J. M. Gaite, J. F. Stenger, Y. Dusausoy, G. Marnier, and H. Rager, J. Phys.: Condens. Matter 3, 7877 (1991).

22. I. N. Gelfman, P. G. Nagornyi, A. N. Usov, and Pham za Ngy, Sov. Phys. Solid State 33, 1535 (1991).

23. S. Han, J. Wang, Y. Xu, Y. Liu, and J. Wei, J. Phys.: Condens. Matter 4, 6009 (1992).

24. I. Tordjman, R. Masse, and J. C. Guittel, Z. Kristallogr. **139**, 103-115 (1974).

25. P. A. Thomas, A. M. Glazer, and B. E. Watts, Acta. Cryst. **B46**, 333-343 (1990).

26. L. E. Halliburton, D. L. Cowan, W. B. J. Blake, and J. E. Wertz, Phys. Rev. B 8, 1610 (1973).

27. A. E. Hughes and B. Henderson, in Point Defects in Solids, edited by James H. Crawford, Jr., and Lawrence M. Slifkin (Plenum, New York, 1972), Vol. 1, Chap. 7, pp. 443-455.

28. K. Tsuchida, R. Abe, and M. Naito, J. Phys. Soc. Jpn. 35, 806 (1973).

29. M. N. Kabler, in Point Defects in Solids, edited by James H. Crawford, Jr., and Lawrence M. Slifkin (Plenum, New York, 1972), Vol. 1, Chap. 6, pp. 329-359.

30. J. L. Shay and J. H. Wernick, Ternary Chalcopyrite Semiconductors: Growth, Electronic Properties, and Applications, (Pergamon Press, New York, 1975).

31. Y. M. Andreev, V. G. Voevodin, A. I. Gribenyukov, O. Y. Zyryanov, I. I. Ippolitov, A. N. Morozov, A. V. Sosnin, and G. S. Khmel'nitskii, Sov. J. Quantum Electron. 14, 1022 (1984).

32. Y. M. Andreev, V. Y. Baranov, V. G. Voevodin, P. P. Geiko, A. I. Gribenyukov, S. V. Izyumov, S. M. Kozochkin, V. D. Pis'mennyi, Y. A. Satov, and A. P. Strel'tsov, Sov. J. Quantum Electron. 17, 1435 (1987).

33. A. M. Prokohorov and Y. S. Kuz'minov, Ferroelectric Crystals for Laser Radiation Control, (Adam Hilger, Bristol, 1990).

34. N. P. Barnes, International Journal of Nonlinear Optical Physics 1, 639 (1991).

35. P. G. Schunemann and T. M. Pollak, in OSA Proceedings on Advanced Solid-State Lasers, edited by George Dube and Lloyd Chase (Optical Society of America, Washington, D.C., 1991) Vol. 10, pp. 332-334.

36. P. A. Budni, P. G. Schunemann, M. G. Knights, T. M. Pollak, and E. P. Chicklis, in OSA Proceedings on Advanced Solid-State Lasers, edited by Lloyd L. Chase and Albert A. Pinto (Optical Society of America, Washington, DC, 1992), Vol. 13, pp. 380-383.

37. P. G. Schunemann, P. A. Budni, M. G. Knights, T. M. Pollak, E. P. Chicklis, and C. L. Marquardt, 1993 Technical Digest Series Volume 2 for Advanced Solid-State Lasers (Optical Society of America, Washington, D.C., 1993), pp. 131-133.

38. H. M. Hobgood, T. Henningsen, R. N. Thomas, R. H. Hopkins, M. C. Ohmer, W. C. Mitchel, D. W. Fischer, S. M. Hegde, and F. K. Hopkins, J. Appl. Phys. 73, 4030 (1993).

39. A. Kiel, Solid State Commun. 15, 1021 (1974).

40. M. D. Lind and R. W. Grant, J. Chem. Phys. 58, 357 (1973).

41. U. Kaufmann, J. Schneider, and A Rauber, Appl. Phys. Lett. 29, 312 (1976).

42. Y. V. Rud and R. V. Masagutova, Sov. Tech. Phys. Lett. 7, 72 (1981).

43. S. C. Abrahams and J. L. Berstein, J. Chem. Phys. 61, 1140 (1974).

44. R. Madelon, E. Paumier, and A. Hairie, phys. stat. sol. (b) 165, 435 (1991).

45. S. Isomura, S. Takahashi, and K. Masumoto, Japan. J. Appl. Phys. 16, 1723 (1977).

46. R. Madelon, M. Shaimi, A. Hairie, E. Paumier, and B. Mercey, Solid State Commun. 50, 545 (1984).

47. G. D. Boyd, E. Buehler, F. G. Storz, and J. H. Wernick, IEEE J. Quantum Electron. QE 8, 419 (1972).

48. G. W. Iseler, H. Kildal, and N. Menyuk, J. Elect. Mat. 7, 737 (1978).

49. H. Kildal, Ph.D. Dissertation, Stanford University (1972); Technical Report AFML-TR-72-277, Wright Patterson Air Force Base, Ohio.

50. M. H. Rakowsky, W. K. Kuhn, W. J. Lauderdale, L. E. Halliburton, G. J. Edwards, M. P. Scripsick, P. G. Schunemann, T. M. Pollak, M. C. Ohmer, and F. K. Hopkins, Appl. Phys. Lett. 64, 1615 (1994).

51. I. Aksenov, N. Nishikawa, and K. Sato, J. Appl. Phys. 74, 3811 (1993).

52. H. J. Bardeleben, A Goltzene, and C. Schwab, phys. stat. sol. (b) 76, 363 (1971).

FIGURE CAPTIONS

Figure 1. EPR spectra from Ti^{3+} centers in x-ray-irradiated hydrothermally grown KTP crystals. Center A_{hyd} is shown in trace (a) and Center B_{hyd} is shown in trace (b).

Figure 2. ENDOR spectrum obtained from Center A_{hyd} with the magnetic field parallel to the b direction.

Figure 3. EPR spectra from Ti^{3+} centers in x-ray-irradiated flux-grown KTP crystals. Center B_{flx} is shown in trace (a) and Center C_{flx} is shown in trace (b).

Figure 4. ENDOR spectrum obtained from Center B_{flx} with the magnetic field parallel to the b direction.

Figure 5. Infrared absorption spectra comparing the OH^- concentrations in hydrothermally grown and flux-grown KTP.

Figure 6. EPR spectra of the trapped-hole center in KTP. The data were taken at approximately 30 K and the magnetic field was aligned, in turn, along each of the crystal's high symmetry directions.

Figure 7. Angular variation (g matrix portion only) of the EPR spectrum of the trapped-hole center. The experimental data are represented by the circles while the solid lines were calculated using the g matrix in Table II.

Figure 8. ENDOR spectrum of the trapped-hole center in KTP taken with the magnetic field along the c axis of the crystal. The measurement temperature was approximately 30 K and the microwave frequency was 9.6627 GHz. Stick diagrams illustrate the three pairs of phosphorus ENDOR lines corresponding to the resolved splittings in the c-axis EPR spectrum shown in Fig.1(a).

Figure 9. Angular variation associated with the largest ^{31}P hyperfine interaction. The circles represent ENDOR data and the solid lines are calculated using the A_1 hyperfine matrix in Table II.

Figure 10. Angular variation associated with the A_2 (dashed lines) and A_3 (solid lines) hyperfine interactions. The circles represent experimental data points and the lines are calculated using the "best-fit" hyperfine matrices in Table II.

Figure 11. Model of the trapped-hole center in KTP. A projection of the lattice on the **a-c** plane is shown with the height of each ion along the **b** direction given in angstroms. The hole is localized in a nonbonding p orbital of an oxygen ion bridging two titanium ions. The p orbital points toward a potassium vacancy (represented by the large square) on one side and toward a phosphorus ion on the opposite side.

Figure 12. EPR spectra taken at 20 K in $ZnGeP_2$ with the magnetic field parallel to the [001], [110], [100], and [011] directions. The "stick diagrams" below each trace indicate the triplet positions.

Figure 13. The four crystallographically equivalent orientations of the EPR-active acceptor in $ZnGeP_2$. The center of the tetrahedron, labeled M, is suggested to be either a zinc vacancy or a zinc on a germanium site.

Figure 14. EPR spectra of as-grown $CdGeAs_2$ taken at 17 K with (a) the magnetic field parallel to the c axis and (b) the magnetic field parallel to the a axis.

Figure 15. EPR spectrum of as-grown $CdGeAs_2$ taken at 41 K with the magnetic field parallel to the c axis.

FIGURE 1

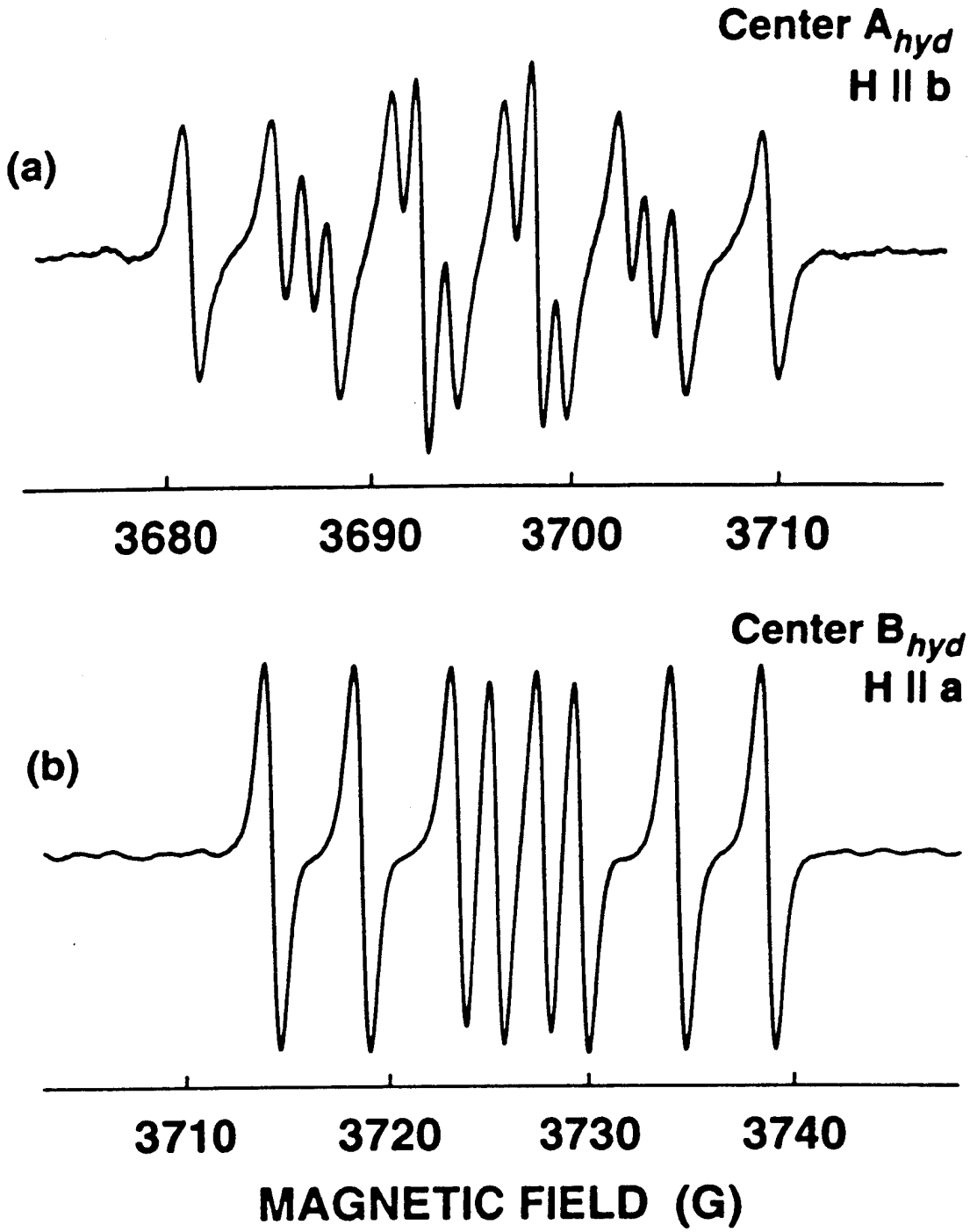
Center A hyd
H II b
(a)
3680
3690
3700
3710
Center B hyd
H II a
(b)
3710
3720
3730
3740
MAGNETIC FIELD (G)

FIGURE 2

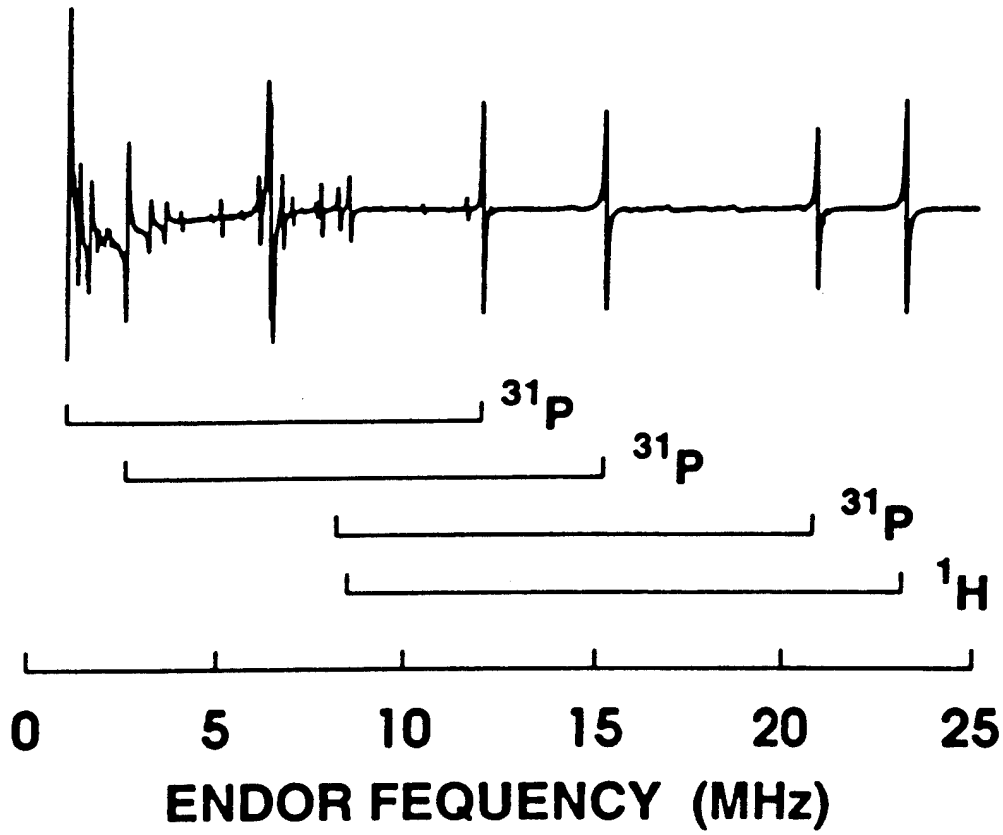

FIGURE 3

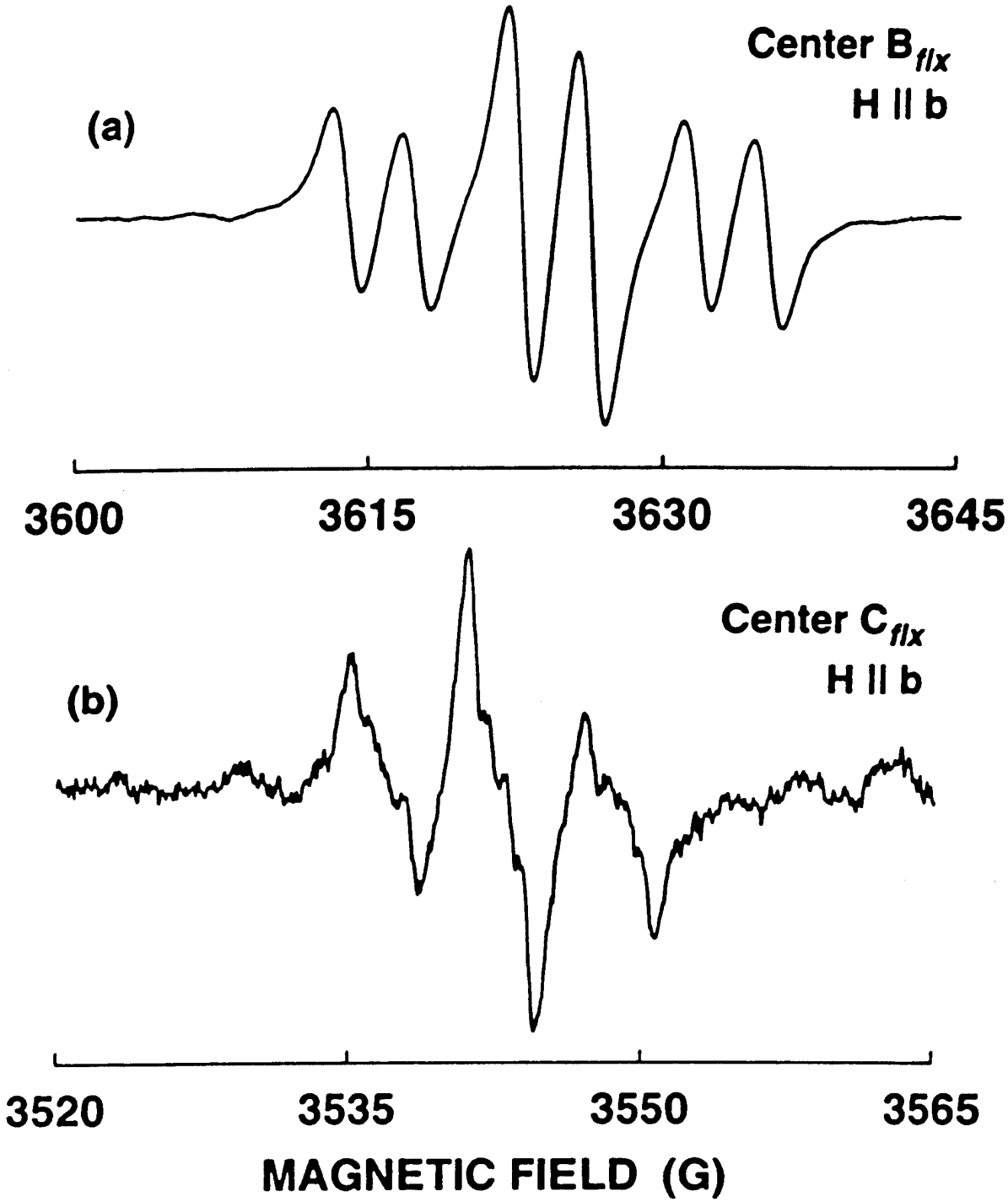
(a)
Center B_{flx}
H ll b
3600
3615
3630
3645
(b)
Center C_{flx}
H ll b
3520
3535
3550
3565
MAGNETIC FIELD (G)

FIGURE 4

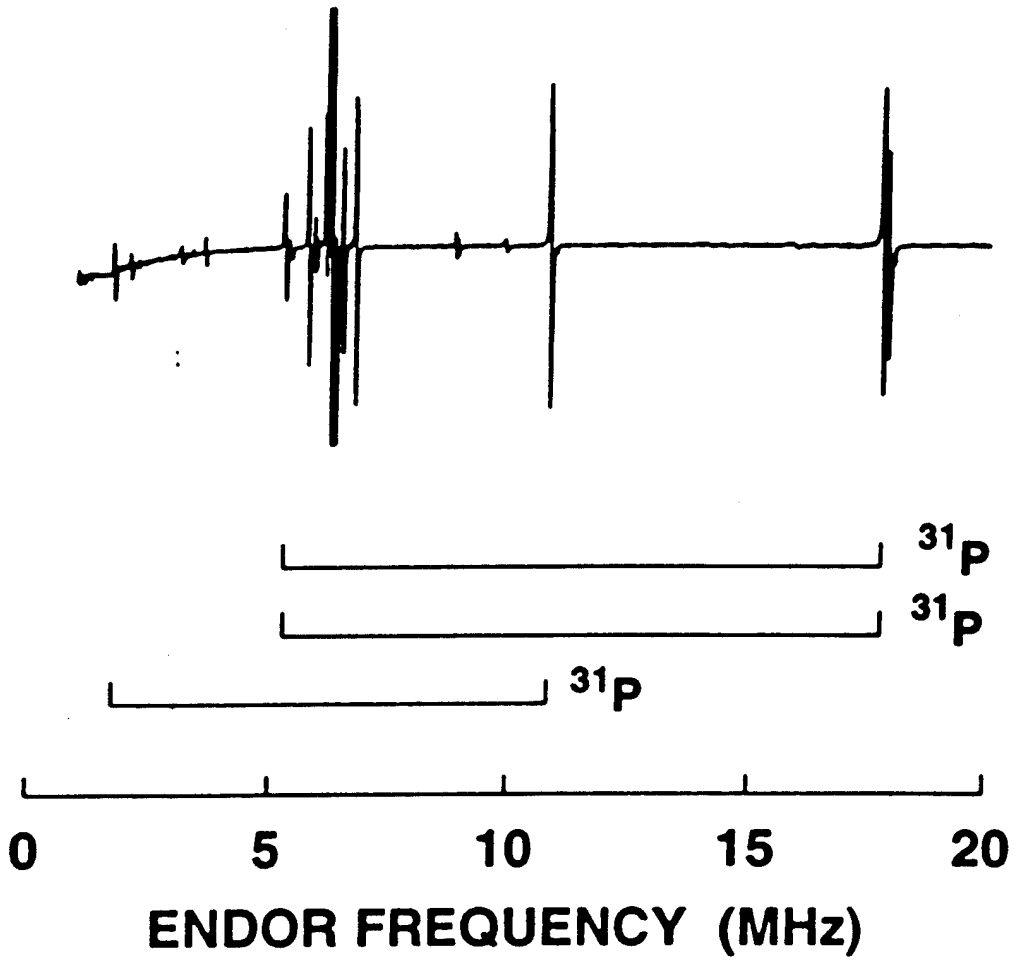

FIGURE 5

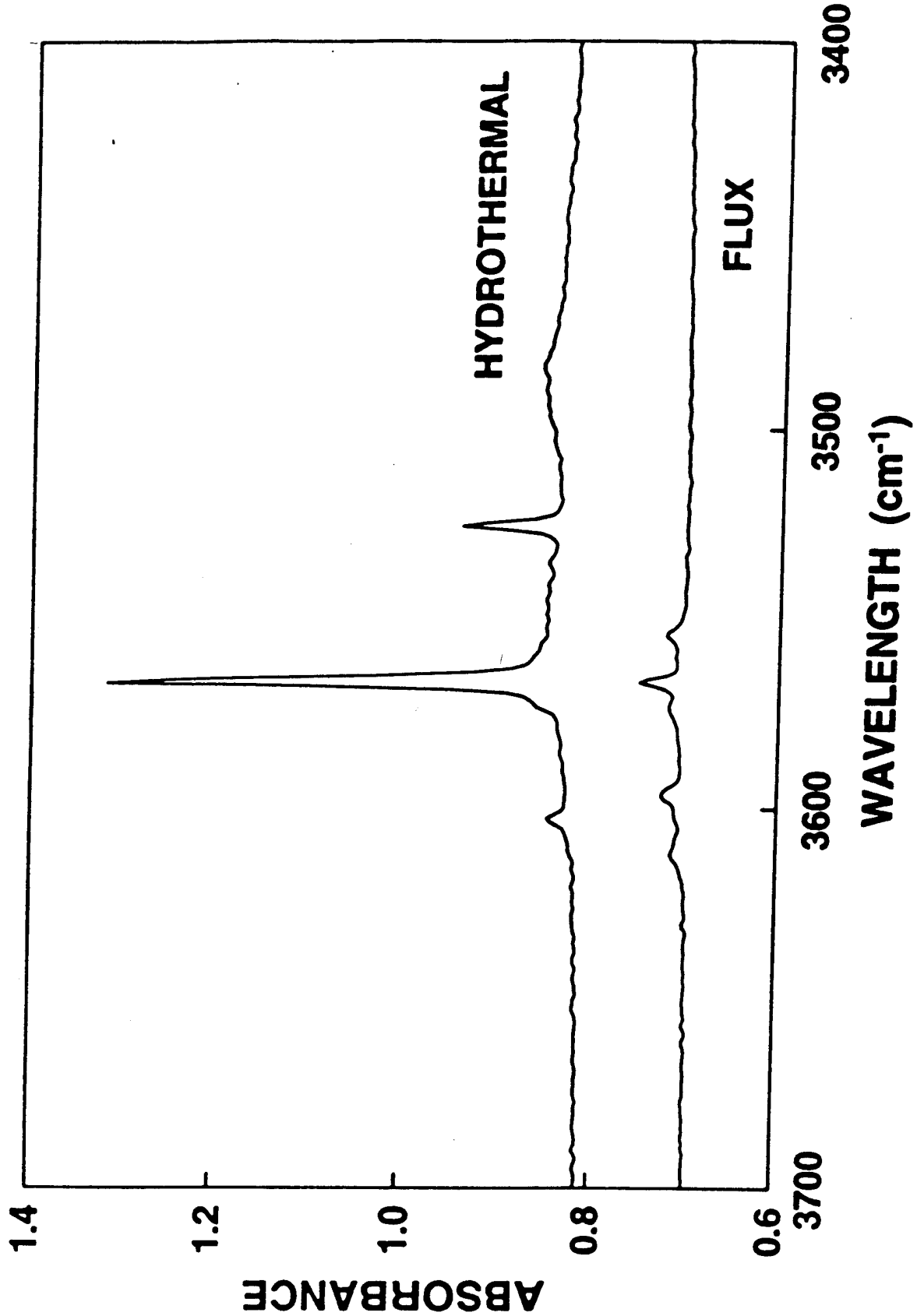
HYDROTHERMAL
FLUX
ABSORBANCE
1.4
1.2
1.0
0.8
0.6
3700
3600
3500
3400
WAVELENGTH (cm-1)

FIGURE 6

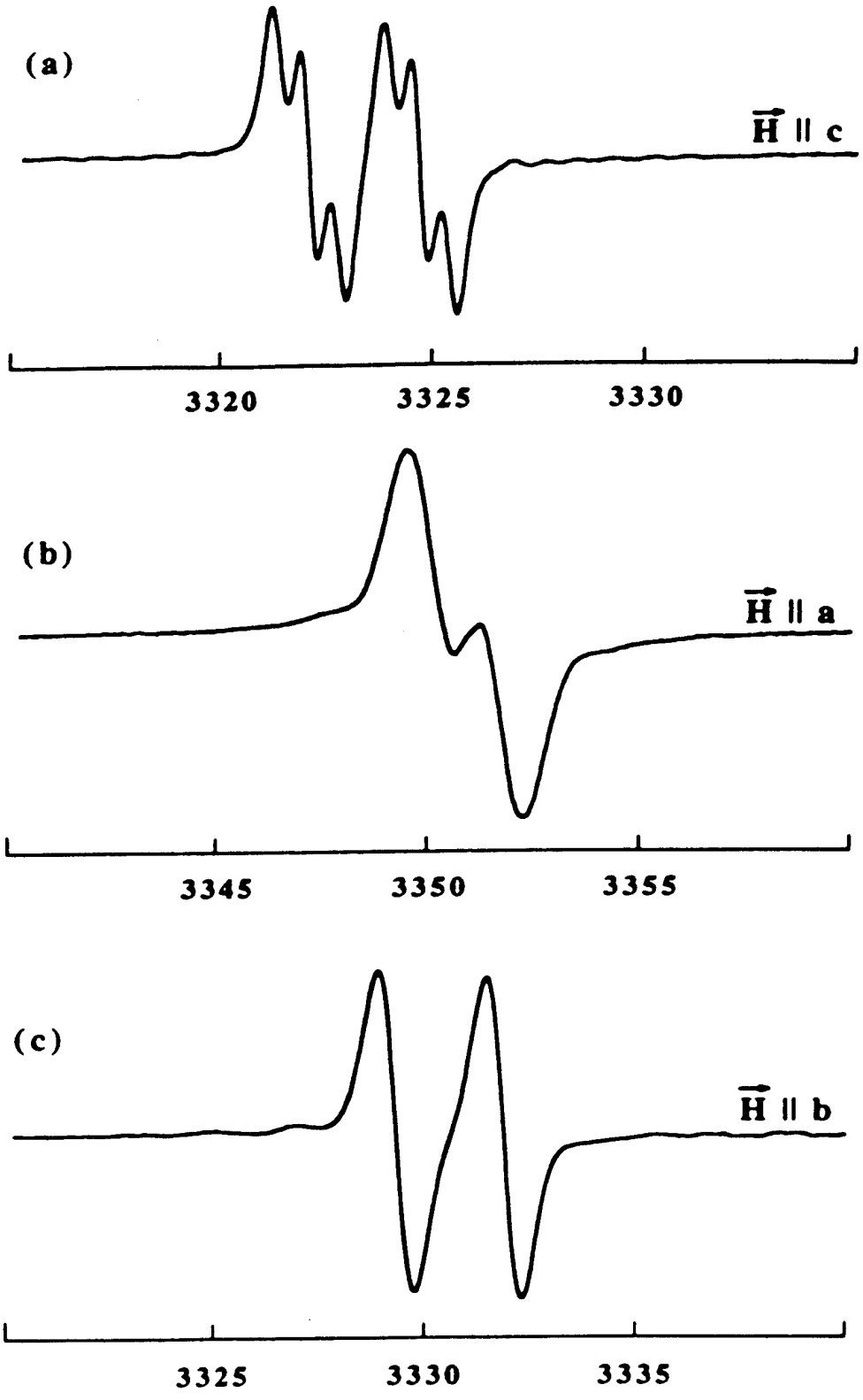
(a)
$\vec{H} \parallel c$
3320
3325
3330
(b)
$\vec{H} \parallel a$
3345
3350
3355
(c)
$\vec{H} \parallel b$
3325
3330
3335
Magnetic Field (Gauss)

FIGURE 7

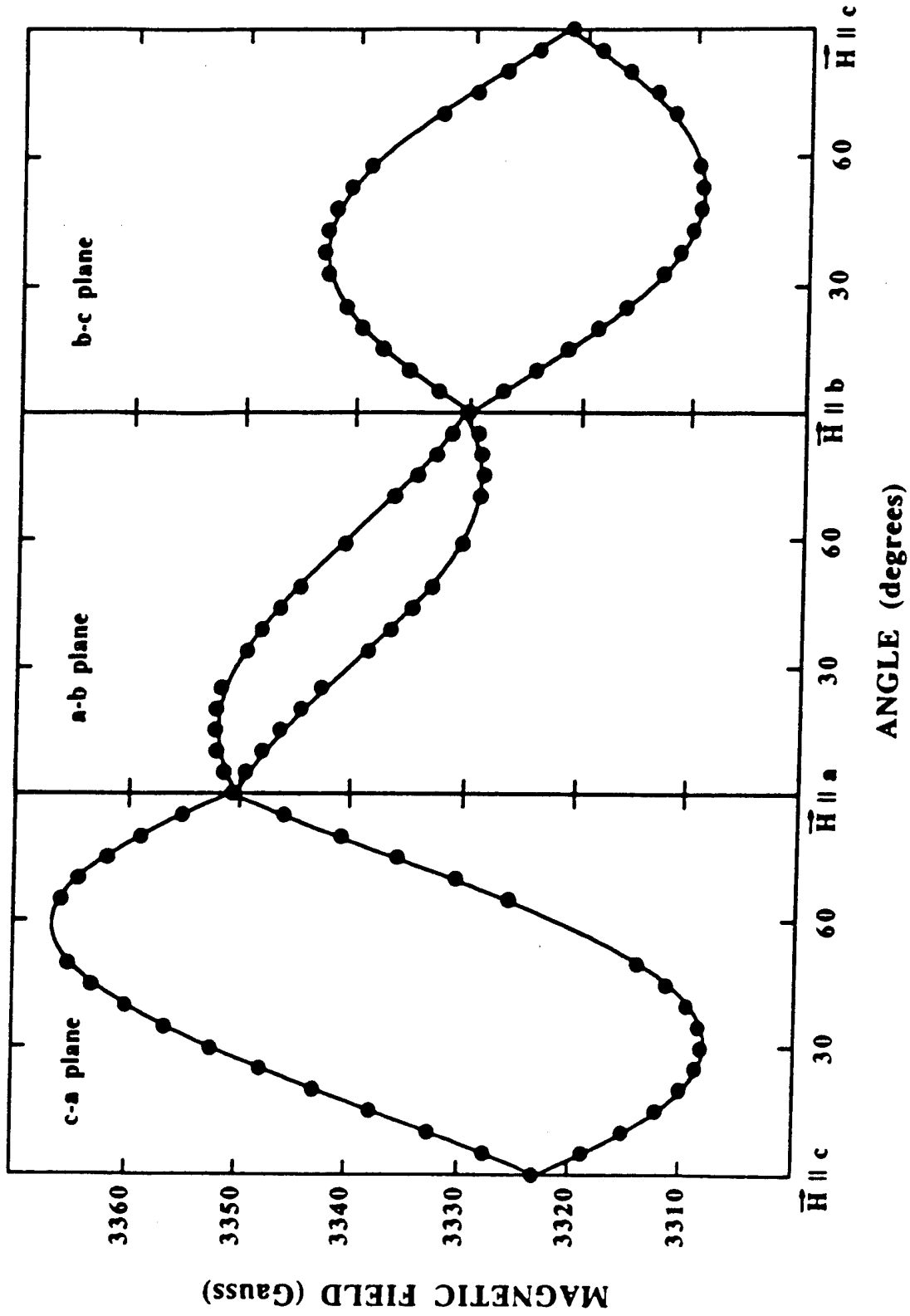
MAGNETIC FIELD (Gauss)
3360
3350
3340
3330
3320
3310
c-a plane
a-b plane
b-c plane
H ∥ c
30
60
H ∥ a
30
60
H ∥ b
30
60
H ∥ c
ANGLE (degrees)

FIGURE 8

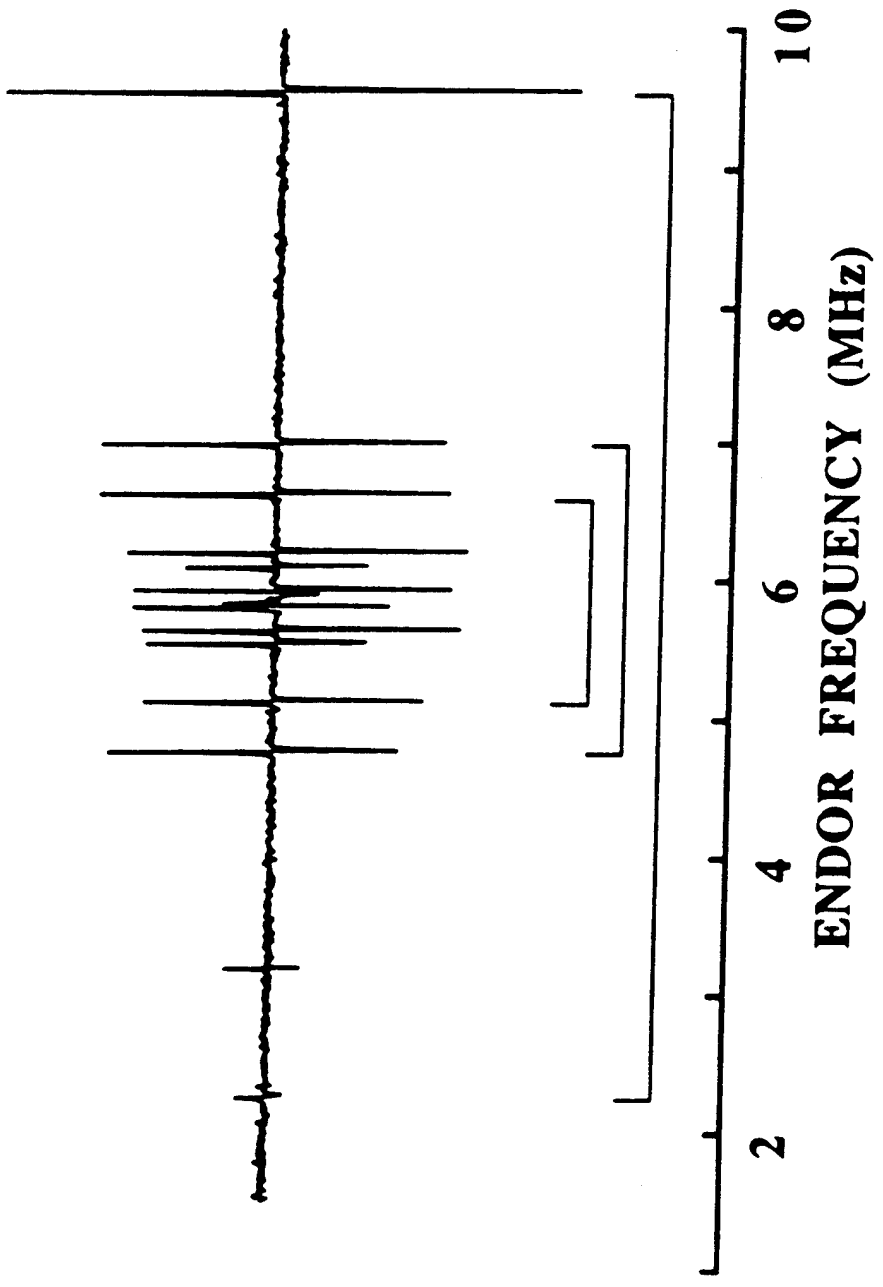

FIGURE 9

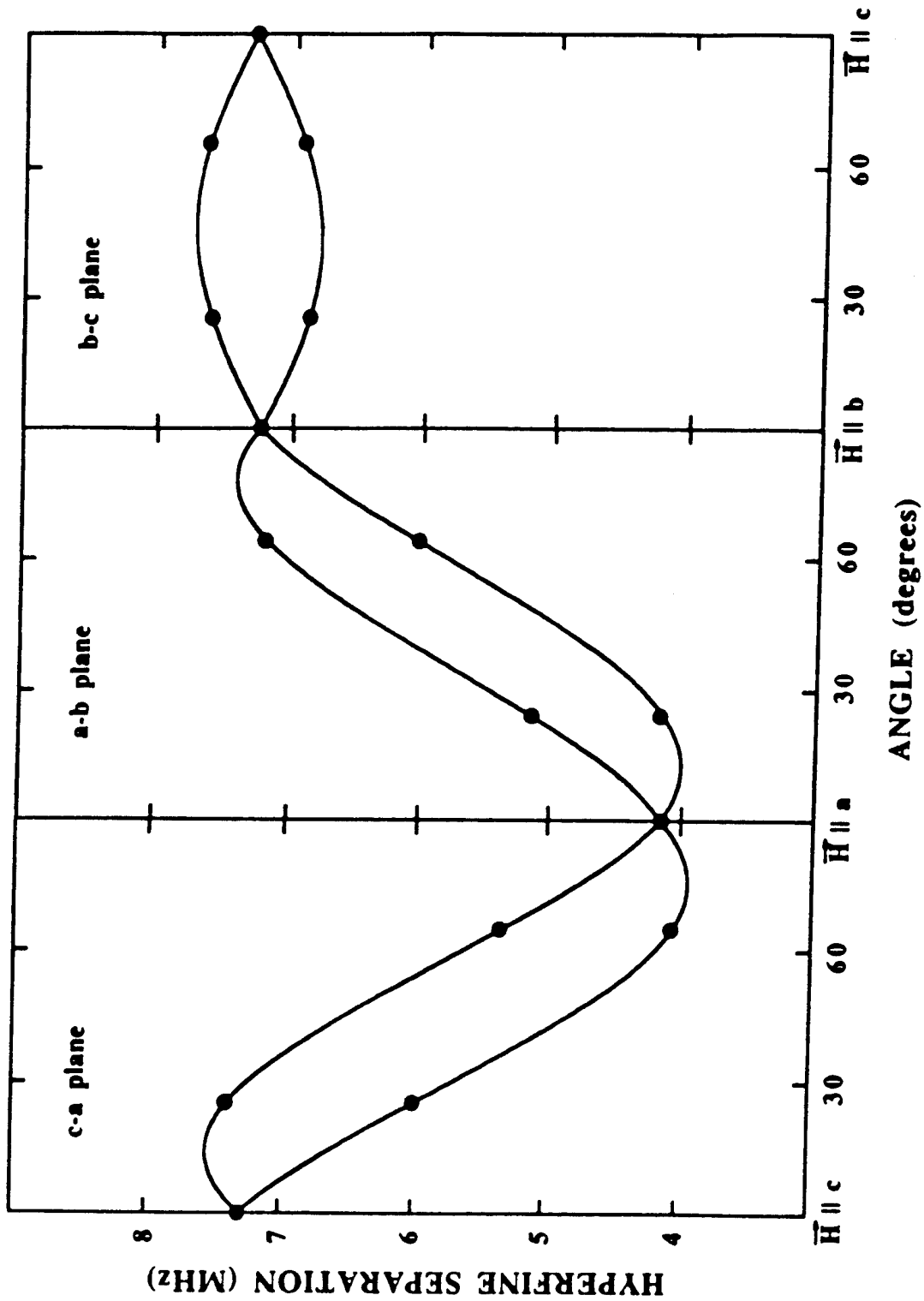
HYPERFINE SEPARATION (MHz)
8
7
6
5
4
c-a plane
a-b plane
b-c plane
H ∥ c
30
60
H ∥ a
30
60
H ∥ b
30
60
H ∥ c
ANGLE (degrees)

FIGURE 10

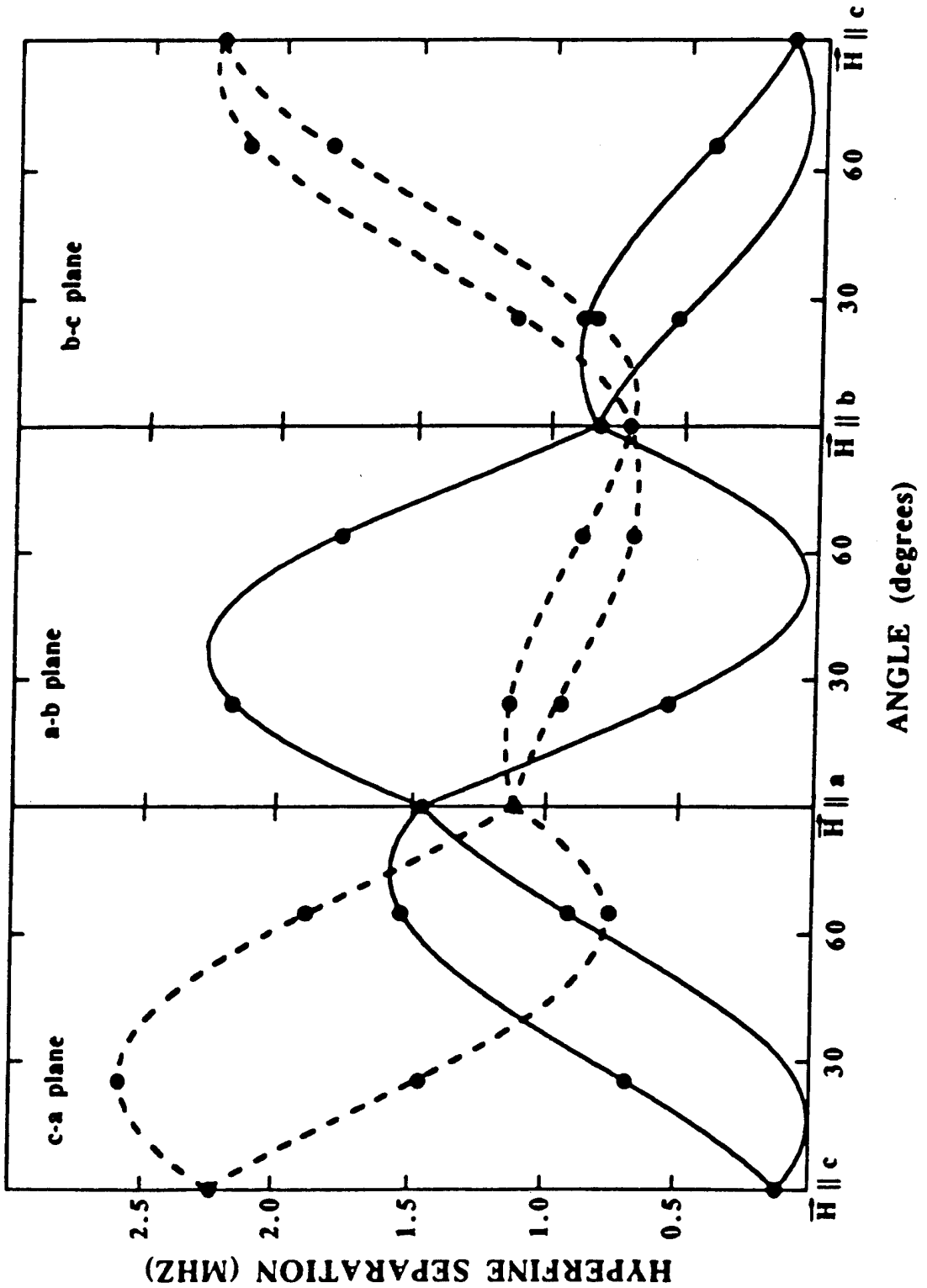
HYPERFINE SEPARATION (MHZ)
2.5
2.0
1.5
1.0
0.5
c-a plane
a-b plane
b-c plane
H ∥ c
H ∥ a
H ∥ b
H ∥ c
30
60
30
60
30
60
ANGLE (degrees)

FIGURE 11

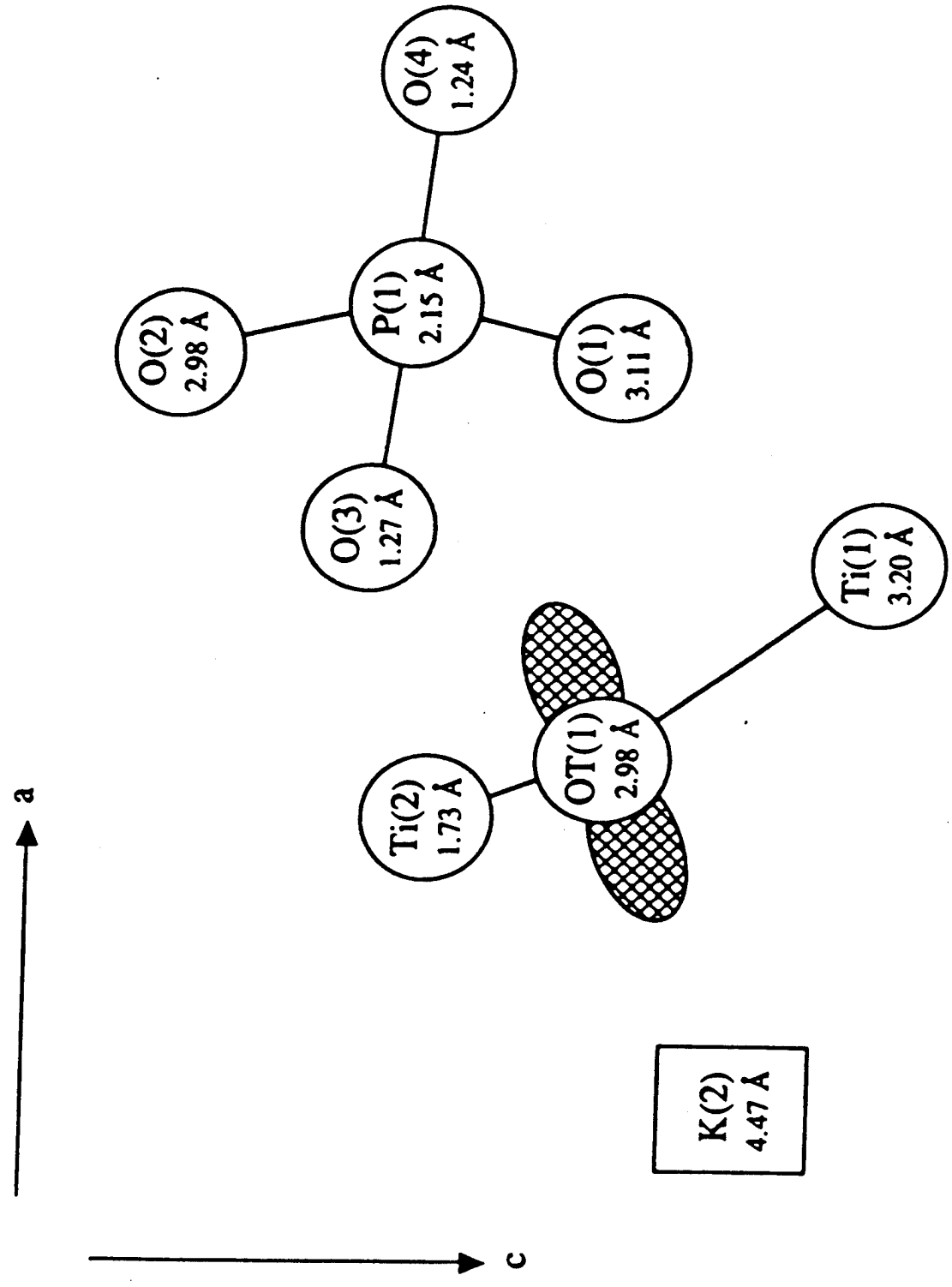
O(4)
1.24 Å
P(1)
2.15 Å
O(2)
2.98 Å
O(1)
3.11 Å
O(3)
1.27 Å
Ti(1)
3.20 Å
OT(1)
2.98 Å
Ti(2)
1.73 Å
K(2)
4.47 Å
a
c

FIGURE 12

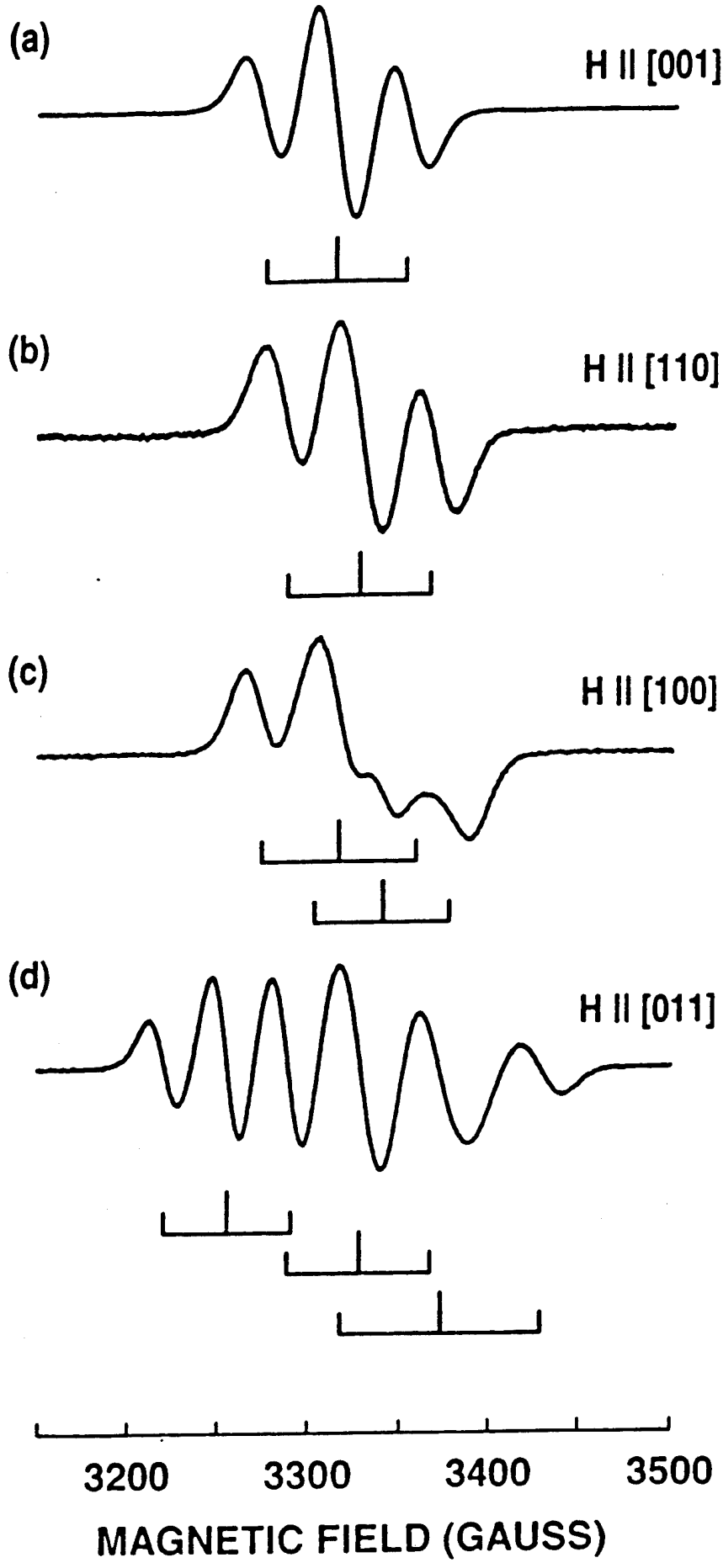
(a)
H II [001]
(b)
H II [110]
(c)
H II [100]
(d)
H II [011]
3200
3300
3400
3500
MAGNETIC FIELD (GAUSS)

FIGURE 13

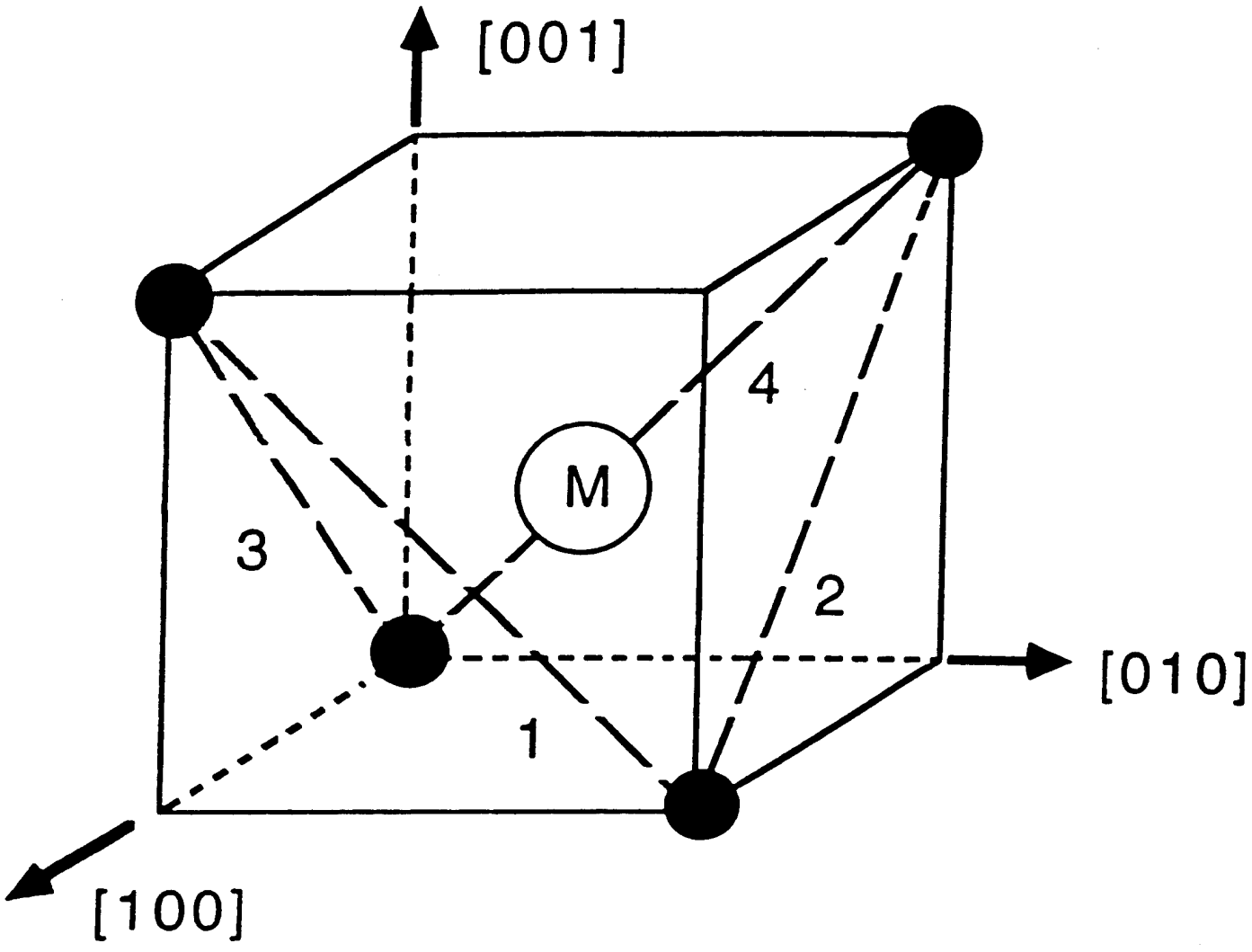

FIGURE 14

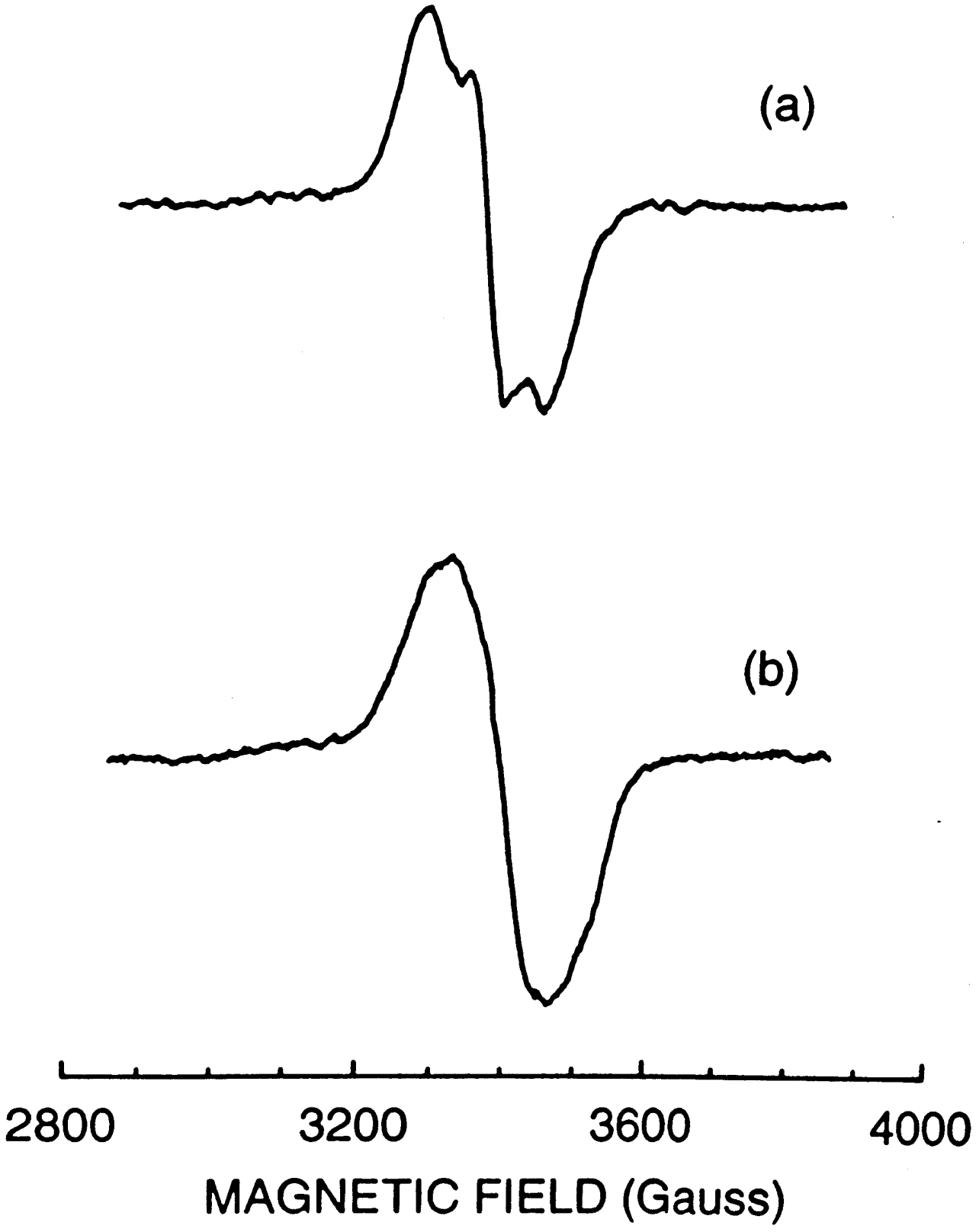

FIGURE 15